Vol. 22, e220008 (2025)
doi: 10.2142/biophysico.bppb-v22.0008

Biophysics and Physicobiology
https://www.jstage.jst.go.jp/browse/biophysico/

Review Article

Genetically-encoded temperature indicators for thermal biology

Tetsuichi Wazawa[1], Ryohei Ozaki-Noma[1,2], Lu Kai[1], Shun-ichi Fukushima[1], Tomoki Matsuda[1,3], Takeharu Nagai[1,2,4]

[1] *SANKEN (The Institute of Scientific and Industrial Research), Osaka University, Ibaraki, Osaka 567-0047, Japan*
[2] *Graduate School of Frontier Biosciences, Osaka University, Suita, Osaka 565-0871, Japan*
[3] *Department of Biosciences, School of Science, Kitasato University, Sagamihara, Kanagawa 252-0373, Japan*
[4] *Transdimensional Life Imaging Division, Institute for Open and Transdisciplinary Research Initiatives, Osaka University, Suita, Osaka 565-0871, Japan*

Received December 14, 2024; Accepted April 3, 2025;
Released online in J-STAGE as advance publication April 8, 2025
Edited by Haruki Nakamura

Temperature crucially affects molecular processes in living organisms and thus it is one of the vital physical parameters for life. To investigate how temperature is biologically maintained and regulated and its biological impact on organisms, it is essential to measure the spatial distribution and/or temporal changes of temperature across different biological scales, from whole organism to subcellular structures. Fluorescent nanothermometers have been developed as probes for temperature measurement by fluorescence microscopy for applications in microscopic scales where macroscopic temperature sensors are inaccessible, such as embryos, tissues, cells, and organelles. Although fluorescent nanothermometers have been developed from various materials, fluorescent protein-based ones are especially of interest because they can be introduced into cells as the transgenes for expression with or without specific localization, making them suitable for less-invasive temperature observation in living biological samples. In this article, we review protein-based fluorescent nanothermometers also known as genetically-encoded temperature indicators (GETIs), covering most published GETIs, for developers, users, and researchers in thermal biology as well as interested readers. We provide overviews of the temperature sensing mechanisms and measurement methods of these protein-based fluorescent nanothermometers. We then outline key information for GETI development, focusing on unique protein engineering techniques and building blocks distinct to GETIs, unlike other fluorescent nanothermometers. Furthermore, we propose several standards for the characterization of GETIs. Additionally, we explore various issues and offer perspectives in the field of thermal biology.

Key words: GETI, nanothermometer, fluorescence microscopy, GFP-like protein

Significance

Temperature is one of fundamental physical parameters for living organisms in that it is associated with various molecular processes in them. To investigate how temperature is relevant to living organisms, genetically-encoded temperature indicators (GETIs) have become important research tools, because they can be exploited for non- or low-invasive measurement of temperature on micrometer and submicrometer scale. This review article describes GETIs as well as their temperature detection mechanisms, development methods, and characterization. Furthermore, we discuss a few critical topics in thermal biology that we expect to be addressed.

Corresponding author: Takeharu Nagai, SANKEN, Osaka University, Ibaraki, Osaka 567-0047, Japan. ORCID iD: https://orcid.org/0000-0003-2650-9895, e-mail: ng1@sanken.osaka-u.ac.jp

Introduction

Temperature is a physical quantity that measures the thermal energy state of an object, and, in biological contexts, governs various molecular processes within organisms. Temperature affects chemical and physical processes and properties, including reaction equilibria and kinetics, phase transitions, liquid fluidity, material elasticity, and both Brownian motion and diffusion. In animals, body temperature is tightly regulated to maintain homeostasis and respond to various stimuli, including stress, infections, and diseases. The regulation of body temperature is closely associated with thermogenesis, including both shivering and non-shivering thermogenesis [1]. Particularly, the non-shivering thermogenesis in mammals is thought to be associated with some physiological aspects such as cold adaptation, fever, hibernation, and obesity [2]. To elucidate how heat is produced within cells and the key roles of thermogenesis across organelles, cells, tissues, and the body of organism, it is essential to image temperature to scrutinize its temporal changes and spatial distribution. Due to the growing need for precise temperature monitoring, various nanothermometers have been developed for temperature observations at the nano and micro scales.

Fluorescent nanothermometers are molecular probes at the nanometer scale capable of reporting temperature through fluorescence [3,4]. Due to their small size and low heat capacity, fluorescent nanothermometers impact the temperatures of cells or organelles of interest to a much less extent than macroscopic sensors like thermocouples and resistance temperature detectors, enabling more accurate and less invasive measurement. Fluorescent nanothermometers have been developed using a variety of materials including organic fluorophores, quantum dots, nanodiamonds, nanoparticles, rare-earth metal complexes, metal nanoclusters, oligonucleotides, polymers, and fluorescent proteins (FPs) [3,4]. Among them, protein-based fluorescent nanothermometers derived from FPs hold significant interest in biological research due to their versatile applications and biocompatibility. Protein-based fluorescent nanothermometers can be genetically encoded and introduced into cells for expression. Thus, protein-based fluorescent nanothermometers are often referred to as genetically-encoded temperature indicators (GETIs). Furthermore, GETIs can be modified through genetic engineering to be fused with various targeting signal peptides and proteins, allowing for specific localization within cells. These features highlight the utility of GETIs for live cell imaging using diverse fluorescence microscopy techniques.

In this review paper, we discuss GETIs developed up to this point, targeting both potential and current users, developers, and those interested in thermal biology. One type of GETI consists of an FP alone or an FP fused with proteins or polypeptides for localization purposes. For this type of GETI, developers have focused on developing accurate and reliable methods to estimate temperature from fluorescence signals. The other type of GETI has been developed using multiple FPs and temperature-responsive polypeptides or proteins. In this article, we discuss both types of GETIs used for fluorescence measurements in cuvettes and cells (Table 1). Furthermore, we describe the temperature sensing mechanisms in GETIs, fluorescence signals obtained from GETIs, development techniques, representative examples, and characterization methods. We also address current challenges in thermal biology. We highlight that, to date, all published GETIs contain one or two green fluorescent protein (GFP)-like proteins [5], and report temperature through fluorescence. Future developments may include bioluminescent GETIs.

Cellular thermogenesis

The temperature within a cell strictly depends on heat transfer, heat absorption, and thermogenesis, considering its volume, density, and heat capacity. A process that produces or supplies heat drives the temperature to increase, whereas one that absorbs or dissipates heat drives it to decrease. The fundamental driving force of intracellular thermogenesis is chemical reactions. Since all chemical reactions are to some extent exothermic or endothermic, the total heat within a cell results from their combined effects. Thus, although metabolic reactions may produce significant amounts of heat, other processes such as signal transduction pathways, ATP turnover involving protein molecular machines, and biosynthesis also contribute to cellular thermogenesis. Additionally, heat transfer generally includes conduction, convection, and radiation; however, within a cell in tissue or culture medium, heat conduction or diffusion is predominant [6].

Considerable effort has been devoted over the decades to measuring cellular heat generation, referred to as heat flux, using calorimetry. Kemp summarized calorimetry data from various animal cells, reporting values ranging from 1 pJ $s^{-1}cell^{-1}$ to 300 pJ $s^{-1}cell^{-1}$ [7]. These heat flux values encompass all intracellular processes that involve heat generation or absorption. Furthermore, to gain insight into cellular thermogenesis, it is worthwhile to examine the heat associated with individual reaction steps or networks of reactions. Alberty and his colleagues conducted a series of systematic thermodynamic studies using the extended Debye-Hückel theory, calculating *formation* Gibbs free energies and enthalpies under physiological conditions (e.g., pH 7, ion strength of 0.1 M, pMg 3, 298.15 K, and 1 Bar) for various biologically relevant compounds based on experimental data, referred to as standard transformed Gibbs free energies and enthalpies of formation [8]) (see ref [9] and references therein). Importantly, Alberty devised a procedure to calculate the standard transformed Gibbs free energies and enthalpies of various reactions based on these values. Here, it is noted that, according to the first law of thermodynamics, an enthalpy change ΔH is expressed as $\Delta H = Q_P + W_{net}$ at constant pressure, where Q_P

Table 1 Development of GETIs and temperature measurement using GETIs in chronological order

GETI	Fluorescence signal	Mechanism of temperature response	Building blocks	Sensitivity %/K
GFP-TlpA [10]	Fluorescence intensity	Conformational change of TlpA	GFP, TlpA	0.82
EGFP [11]	Relaxation time of fluorescence blinking	Chromophore protonation and deprotonation	EGFP	–4.8
EGFP, DsRed1 [12]	Fluorescence intensity	Thermal quenching	EGFP, DeRed1	–1.7 (GFP) –1.0 (DsRed1)
EGFP, GFP-GAD [13,14]	Fluorescence polarization anisotropy	Rotational Brownian motion	EGFP, glutamic acid decarboxylase	0.1 (GFP in buffer) 0.4 (GFP-GAD in cells)
tsGFP [15]	Dual-band excitation ratio	Conformation change of TlpA	GFP, TlpA	–3.92 (tsGFP1), –3.87 (tsGFP2)
mRFP1 [16]	Fluorescence intensity	Thermal quenching	mRFP1, mRFP-P63A	−1.27 (mRFP1), −1.26 (mRFP-P63A), −0.77 (mRFP-P63A[(4R)-FP])
gTEMP [17]	Dual-band emission ratio	Thermal quenching	Sirius, mt-Sapphaire, T2A	2.6
wt-GFP, emGFP-mito [18]	Peak fraction	Emission thermochromism	wt-GFP, CellLight BacMam 2.0 Mitochondria-emGFP	0.26 (wt-GFP) 2.5 (emGFP-mito)
OCP-TagGFP, TagRFP-OCP [19]	Relaxation rate of fluorescence intensity	Conformational relaxation of OCP	Orange carotenoid protein, TagGFP, TagRFP	10.4 (OCP-TagGFP) 14.7 (TagRFP-OCP)
Actin-GFP [20]	Fluorescence lifetime	Thermal quenching	Actin-GFP	0.23
ELP-TEMP [21]	Dual-band emission ratio	Coacervation of ELP, FRET	mTurquoise2, mVenus, elastin-like polypeptide	45.1
B-gTEMP [22]	Dual-band emission ratio	Thermal quenching	mNeonGreen, tdTomato	1.6
DFPTB [23]	Dual-band emission ratio	Thermal quenching	GFP, mCherry	6.7
gMELT [24]	Dual-band emission ratio	Conformation change of $TlpA_{99\text{-}359}$, FRET	cp173mTurquoise2, cp173mAchilles, $TlpA_{99\text{-}359}$ mutants	39.3 (cytoplasm), 33.8 (ER), 22.0 (mitochondria)

is the heat supplied to the system at constant pressure and W_{net} is the net non-PV work done on the system [25]. Thus, if the magnitude of W_{net} is negligible and the pressure is constant, then $\Delta H = Q_P$, indicating that an enthalpy change can be

used to estimate heat production or absorption for a given process. Furthermore, the standard transformed enthalpy of *reaction* $\Delta_r H'^\circ$ is calculated as

$$\Delta_r H'^\circ = \sum_i \nu_i \Delta_f H_i'^\circ , \quad (1)$$

where ν_i is the stoichiometric coefficient ($\nu > 0$ and $\nu < 0$ for products and reactants, respectively) and $\Delta_f H_i'^\circ$ is the standard transformed enthalpy of formation for compound *i*. For example, using $\Delta_f H'^\circ$ values for ATP, ADP, phosphate, and H_2O of −2979.02, −1996.15, −1299.42, and −286.45 kJ mol^{-1}, respectively, at pH 7, pMg 3, ion strength of 0.1 M, 298.15 K, and 1 Bar [9], $\Delta_r H'^\circ$ for the ATP hydrolysis reaction (ATP + H_2O → ADP + phosphate) is calculated to be −30.1 kJ mol^{-1}, indicating an exothermic reaction. Additionally, for glycolysis with lactate as the final product (glucose + 2 ADP + 2 phosphate → 2 lactate + 2 ATP + 2 H_2O), $\Delta_r H'^\circ$ is calculated to be −49.65 kJ mol^{-1}. In this manner, $\Delta_r H'^\circ$ for many other reactions can be estimated under specific conditions of pH, pMg, ionic strength, and temperature, as described in ref [9]. Previously, we applied Alberty's procedure to analyze the metabolic heat of the β-oxidation and the electron transfer chain, and compared it with Joule heating caused by H^+ leak through uncoupling protein 1 (UCP1) in brown adipose tissue mitochondria (BATM) [26].

Although numerous chemical reactions in cells involve heat production or absorption, several thermogenic mechanisms that produce significant amounts of heat have been identified not only in homeothermic animals but also in fish and plants. Thermogenic mechanisms often include a 'futile' cycle, in which a substrate is continuously consumed to generate heat as long as is the cycle remains active and the substrate is available. Historically, biological thermogenesis has been categorized into shivering and non-shivering thermogenesis. Shivering thermogenesis relies on the tremor of skeletal muscle, which is associated with increased ATP turnover by actomyosin and the sarco/endoplasmic reticulum Ca^{2+}-ATPase (SERCA) pump, as well as metabolic rate above the basal level [1,27,28]. Non-shivering thermogenesis does not involve such muscle movement and includes various types of mechanisms [29,30]. Non-shivering thermogenesis involving UCP1 in BATM, especially in small mammals, has been extensively investigated. In this mechanism, H^+ leak through the inner mitochondrial membrane mediated by UCP1 is associated with a rise in metabolism rate [31,32]. In skeletal muscle, the uncoupling of the SERCA pump by sarcolipin has been proposed as a non-shivering thermogenesis mechanism, particularly in large mammals such as adult rabbits, dogs, marsupials, and humans [28]. UCP1 is also found in plant mitochondria and is believed to be involved in thermogenesis in potato, Arabidopsis, and skunk cabbage [33]. In plants, another mitochondrial protein, alternative oxidase, which catalyzes the oxidation of ubiquinol and the reduction of oxygen to water while uncoupling the electron transfer chain, is also thought to contribute to thermogenesis [34]. Additionally, artificial protonophores, also known as proton uncouplers or proton translocators, such as carbonyl cyanide p-trifluoromethoxyphenylhydrazone (FCCP) and carbonyl cyanide m-chlorophenylhydrazone (CCCP) have been used to stimulate cells to observe thermogenesis in temperature imaging studies [35–39]. FCCP and CCCP are known to catalyze proton uniport across the inner mitochondrial membrane, driven by the membrane potential and pH gradient, a process referred to as protonophore cycling [40]. However, the detailed molecular mechanism underlying heat production in this context remains elusive.

Mechanisms of temperature sensing in GETIs

In measurement using a GETI, we aim to accurately estimate the temperature of an object of interest. The object can be tissues, culture cells, organelles, protein complexes within cells, or an aqueous solution in a cuvette, with the GETI either dispersed in or in contact with these targets. We measure the fluorescence signal of the GETI, which varies as a function of temperature, and then, estimate the temperature using a fluorescence signal-to-temperature calibration standard (Figure 1A,B). Regarding GETIs, the fluorescence signal can manifest as fluorescence intensity, ratio, lifetime, polarization anisotropy, or fluctuation. Ideally, a GETI's mechanism ensures that the fluorescence signal is a unique and direct function of temperature. The mechanisms employed by GETIs to date are as follows:

(1) Thermal quenching of fluorescence protein
(2) Temperature-dependent shift of emission spectrum of FP
(3) Temperature-dependent rotational Brownian motion of FP
(4) Temperature-induced change of conformation or protein-protein interaction

Thermal quenching, temperature-induced spectral shift, and temperature-dependent rotational Brownian motion are straightforward responses of fluorescence to temperature. The temperature-induced protein-protein interaction or conformation transition can be a response of an FP or a non-FP portion included in a GETI. Thus, for the latter type, mechanisms for converting such events into fluorescence a signal change are incorporated, including Förster resonance

energy transfer (FRET) [41] and protonation/deprotonation of the FP chromophore [42]. In this section, we describe some mechanisms for temperature sensing used in GETIs.

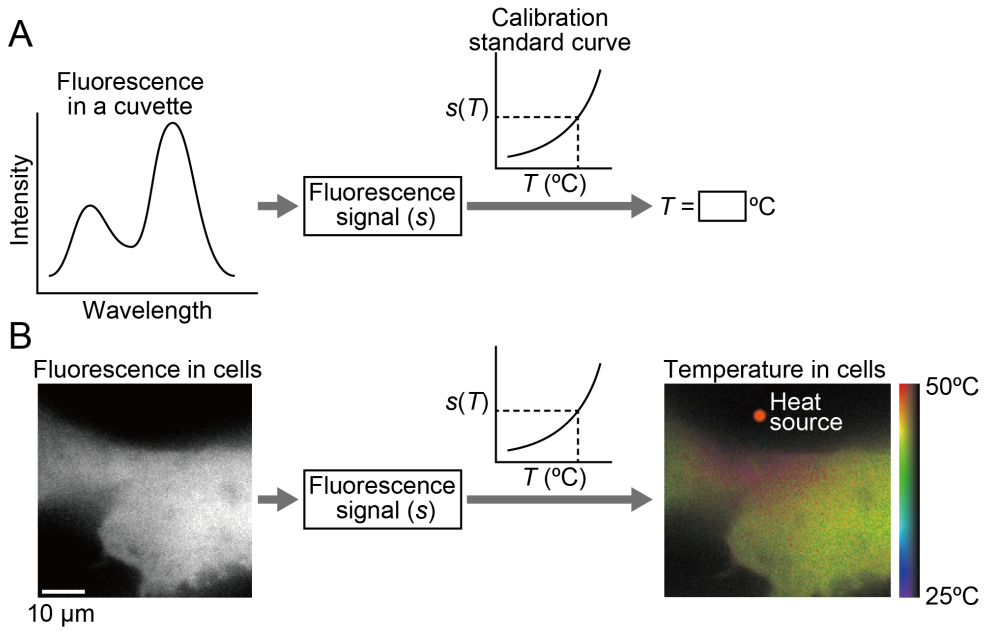

Figure 1 Schematic illustrations of procedures of temperature measurement using GETIs. (A) Measurement of temperature in a cuvette by spectroscopy. A fluorescence signal is extracted from the GETI fluorescence, and the temperature is estimated in reference to the fluorescence signal/temperature standard calibration curve. (B) Measurement of temperature in cells by fluorescence imaging, in which the cells expressing a GETI are heated using a micrometer-sized heat source.

Thermal fluorescence quenching

The fluorescence intensity of an FP is affected by various processes, including temperature-dependent ones. In FPs, particularly GFP-like proteins, fluorescence brightness denoted as $\phi \cdot \varepsilon$ is commonly used to measure intrinsic fluorescence intensity, where ϕ represents the fluorescence quantum yield, and ε represents the molar extinction coefficient. Generally, the temperature change of molar extinction coefficient ε around room temperature may be minimal, provided that the FP remains in its folded conformation, because light absorption accompanies a transition from the electronic ground state to the excited Franck-Condon state (Abs in Figure 2), which precedes relaxation processes such as the vibrational and orientational relaxation of atoms and molecules around the chromophore [43]. The fluorescence quantum yield is described by

$$\phi = \frac{k_r}{k_r + k_{nr}}, \tag{2}$$

where k_r and k_{nr} are rate constants for the radiative and nonradiative deactivation of the excited state, respectively. Radiative deactivation occurs in a single-step, resulting in the emission of a fluorescence photon, the wavelength of which corresponds to the energy gap between the initial and final states (Fl in Figure 2), and thus, the rate constant k_r is thought not to be highly dependent on temperature.

Processes that contribute to the increase of k_{nr} and thus decrease of the fluorescence quantum yield ϕ are termed the fluorescence quenching. Specifically, thermal fluorescence quenching, also known as thermal quenching, is a type of fluorescence quenching mainly characterized by an increase in k_{nr} with temperature. The fluorescence quantum yield of a chromophore of GFP-like protein, 4-(p-hydroxybenzylidene)-5-imidazolinone (p-HBI), dissolved in solvents such as DMSO, ethanol, or H_2O, was reported as being <0.0001 [44], whereas that for a GFP-like protein can be >0.1 (e.g., ϕ = 0.79, 0.6, and 0.8 for wtGFP, EGFP, and mNeonGreen, respectively [45–47]). The nonradiative deactivation encompasses processes such as internal conversion, intersystem crossing, FRET, and quencher-induced quenching (Figure 2) [41,43], with the rate of nonradiative deactivation described as

$$k_{\mathrm{nr}} = \sum_i k_{\mathrm{nr},i} \ , \tag{3}$$

where $k_{\mathrm{nr},i}$ is a rate constant for deactivation process i. In particular, the internal conversion is a nonradiative transition between vibronic states of the same total energy, i.e., isoenergetic states and the same multiplicity (e.g., from the S_1 state to the S_0 state; IC in Figure 2), and the intersystem crossing involves a spin-forbidden nonradiative transition between isoenergetic states of different multiplicity (e.g., from the S_1 state to the T_1 state; ISC in Figure 2) [43,48].

The nonradiative deactivation of GFP-like protein has been investigated using spectroscopy and QM/MM simulation of p-HBI and its derivatives. For the chromophore of GFP-like proteins, intersystem crossing is considered almost negligible, while internal conversion is considered the main route in the nonradiative deactivation of the S_1 state [49]. As demonstrated in previous studies on the p-HBI chromophore, the phenolate and imidazolinone rings in the excited S1 state form an electron donor-acceptor system and can transition to the twisted intramolecular charge transfer (TICT) state [50,51]. As the TICT state is energetically proximate to the S_1/S_0 conical intersection seams, internal conversion from the S_1 to S_0 state predominantly occurs through these intersections, followed by vibrational relaxation to lower energy S_0 vibronic states. In contrast to the p-HBI chromophore alone, the phenolate and imidazolinone rings of p-HBI within a GFP-like protein are substantially immobilized due to steric hindrance and hydrogen bonds from surrounding amino acids and water molecules, significantly impeding the formation of the TICT state, and thus, a high fluorescence quantum yield is achieved. According to this view, a temperature increase should enhance the dynamics of chromophore rings, leading to an increased rate of internal conversion from the S_1 to S_0 state. This enhanced internal conversion would bring about thermal quenching, resulting in decreased fluorescence intensity and fluorescence lifetime. Among GETIs, EGFP, DsRed1, mRFP1, gTEMP, actin-GFP, B-gTEMP, and DFPTB, thermal quenching was utilized to measure temperature (Table 1) [12,16,17,20,22,23].

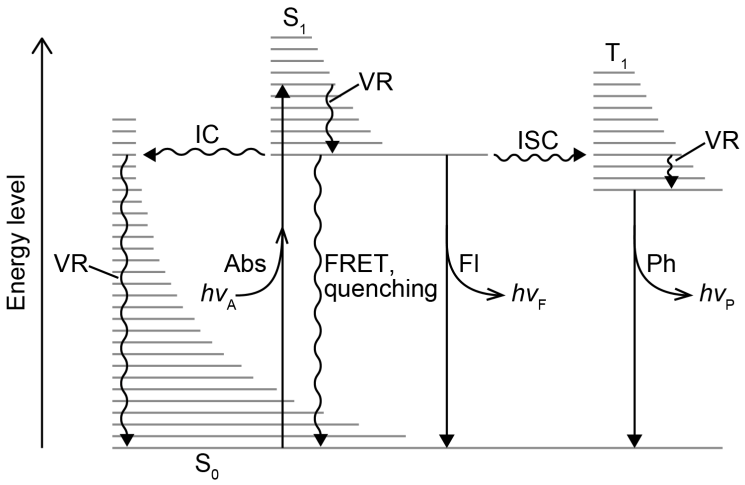

Figure 2 Jablonski diagram depicting the energy levels of the ground state (S_0) and the excited states (S_1 and T_1) of a fluorescent molecule and its relevant photo processes. Abs, photon absorption; Fl, fluorescence; VR, vibrational relaxation; IC, internal conversion; ISC intersystem crossing; Ph, phosphorescence; FRET, Förster resonance energy transfer.

Temperature-dependent shift of fluorescence emission spectrum

GFP has been reported to exhibit a red-shift in the fluorescence emission spectrum with increased temperature [18,52]. Such shift in the emission spectrum was exploited for temperature measurement and imaging [18]. Upon excitation, the chromophore dipolar moment increases due to charge transfer between the phenolate and imidazolinone rings (see **Thermal fluorescence quenching**), leading to rearrangement of its interaction with surrounding atoms and water molecules [52]. The red-shift in the emission spectrum indicates a relaxation process associated with enhanced dynamics of surrounding atoms and water molecules due to increased temperature [41].

Fluorescence depolarization and rotational Brownian motion

The excitation of a fluorescent molecule by linearly-polarized light occurs in a manner dependent on the molecule's orientation relative to the light's polarization vector. Specifically, the probability of excitation is proportional to $\cos^2\theta$, where θ is an angle between the absorption transition dipole moment of the fluorescent molecule and the polarization vector of the excitation light (Figure 3A), a phenomenon known as photoselection [41]. A fluorescent molecule colliding with surrounding molecules undergoes rotational Brownian motion or rotational diffusion whenever in the ground and excited states. Following photoselection, the excited state of fluorescent molecules, typically with a lifetime of nanoseconds, undergoes disordering in their orientation, leading to a decrease in the degree of polarization of fluorescence

(Figure 3B). Because temperature governs rotational Brownian motion, measuring fluorescence polarization can provide insights into the temperature within samples containing fluorescent molecules. Previously, EGFP and GAD-GFP were utilized for temperature measurement via fluorescence polarization anisotropy [13,14]. Herein, we consider the measurement of fluorescence polarization using the schematic configuration shown in Figure 3B.

When vertically polarized continuous light (Excitation light in Figure 3B) is incident on fluorescent molecules in a sample, the fluorescence emitted usually contains both vertically and horizontally polarized components (Fluorescence in Figure 3B). The decrease in fluorescence polarization relative to the excitation light, known as fluorescence depolarization, is primarily caused by rotational Brownian motion on a nanosecond scale and the randomized orientation of fluorescent molecules in the sample. The degree of fluorescence polarization is often evaluated through the steady-state fluorescence polarization anisotropy r, defined as

$$r = \frac{F_V - F_H}{F_V + 2F_H}, \tag{4}$$

where F_V and F_H are the fluorescence intensities for the vertical and horizontal polarization components, respectively, when excited with the vertically-polarized light (Figure 3B). A high value of r corresponds to polarized fluorescence, and a value of r near to zero corresponds to depolarized fluorescence. In particular, if the fluorescent molecules in the sample are randomly oriented, then the fluorescence polarization anisotropy r is ≤0.4.

The fluorescence polarization anisotropy of a sample containing spherical fluorescent molecules, by an approximation, is described by the Perrin equation given as

$$\frac{1}{r} = \frac{1}{r_0} + \frac{\tau_F}{r_0 \tau_R}, \tag{5}$$

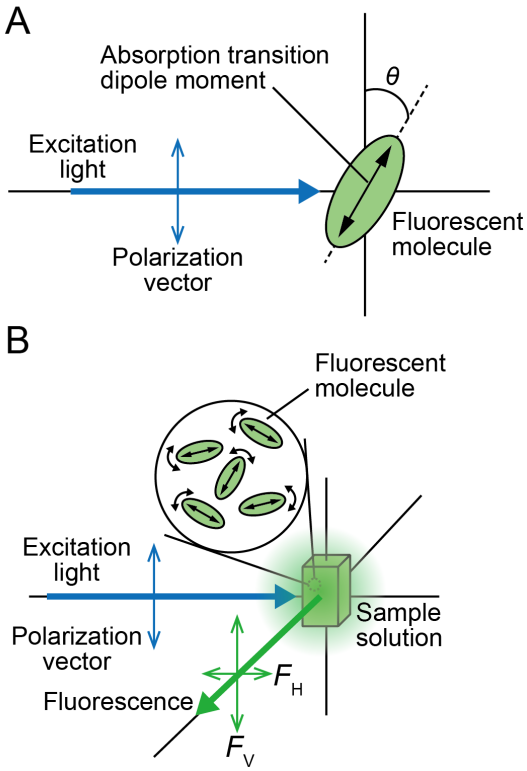

Figure 3 Schematic illustrations of fluorescence polarization anisotropy. (A) Irradiation of a fluorescent molecule with a vertically linearly polarized excitation light. (B) A schematic illustration of an example of fluorescence polarization anisotropy measurement. F_V, vertical polarization component of the fluorescence; F_H, horizontal polarization component of the fluorescence.

where r_0 is the fundamental anisotropy or the zero-time anisotropy, and τ_F and τ_R are the fluorescence lifetime and the rotational correlation time, respectively [41]. The rotational correlation time relates to the rotational diffusion coefficient in a manner such that $\tau_R = 1/(6D_R)$ [53,54], and the rotational diffusion coefficient D_R is described by the Stokes-Einstein-Debye equation as

$$D_R = \frac{k_B T}{8\pi\eta R_h^3} = \frac{k_B T}{6\eta V_h}, \tag{6}$$

where k_B, T, and η are the Boltzmann constant, absolute temperature, and the viscosity of the microenvironment around the fluorescent molecules, respectively, and R_h and V_h are the radius and the volume, respectively, of the hydrated fluorescent molecules [55]. Accordingly, the fluorescence polarization anisotropy r can be used as a measure of temperature T, although r is also affected by the viscosity η, which is also dependent on T.

Additionally, the fluorescence polarization anisotropy of a fluorescent dye or chromophore tethered to a larger host molecule such as protein may deviate from the Perrin equation (Equation (5)), suggesting complex rotational dynamics. The fluorescence polarization anisotropy of this situation may be affected not just by the restricted rotational Brownian motion of the chromophore but also by the rotational Brownian motion of the host molecule, and this can be explained by models such as the wobbling-in-cone model [56–58]. However, in the case of GFP, the chromophore of p-HBI is

embedded in the protein portion [42], and the time-resolved anisotropy decay was well described by a single exponential function [59]. Thus, the contribution of the chromophore's local wobbling motion to the overall fluorescence polarization anisotropy is considered to be minimal. Accordingly, for the steady-state fluorescence anisotropy of GFP-like proteins, the Perrin equation (Equation (5)) serves as an effective approximation, reflecting the minimal impact of chromophore dynamics within the protein structure.

Protein-protein interaction and conformation change

Several GETIs contain temperature sensing domains composed of non-fluorescent protein (non-FP) portions that undergo conformational changes and/or protein-protein interactions in response to temperature. The GETIs include GFP-TlpA, tsGFP, ELP-TEMP, OCP-TagGFP, TagRFP-OCP, and gMELT (Table 1) [10,15,19,21,24]. The temperature sensing domains are as follow: TlpA for GFP-TlpA, tsGFP, and gMELT; elastin-like polypeptide (ELP) for ELP-TEMP; orange carotenoid protein (OCP) for OCP-TagGFP and TagRFP-OCP [60–62]. In these GETIs, a conformational change and/or protein-protein interaction in response to temperature are coupled to a mechanism responsible for fluorescence signal changes. The mechanisms involved in the conversion of temperature-induced changes to fluorescence signal changes include FRET and the protonation/deprotonation equilibrium of chromophore. ELP-TEMP, OCP-TagGFP, TagRFP-OCP, and gMELT utilize FRET, whereas GFP-TlpA and tsGFP are based on the protonation/deprotonation equilibrium of the chromophore.

TlpA, an α-helical protein, was identified from the large virulence associated plasmid of *Salmonella enterica* subsp. enterica serovar Typhimurium (or Salmonella typhimurium) [60]. Like other coiled-coil proteins, TlpA contains heptapeptide repeats of *a-b-c-d-e-f-g*, with *a* and *d* being hydrophobic amino acid residues [60]. TlpA exists as a randomly-coiled monomer at high temperatures (>40 °C) and as a coiled-coil dimer at low temperatures (< 40 °C) [10,63]. The transition between these two states is highly reversible in repeated cycles of heating and cooling, and the kinetics is relatively fast (< min) [10]. Furthermore, TlpA was engineered to enable its variants to respond to specific temperatures and form particular heterodimers [64,65].

Elastin-like polypeptides (ELPs) are a class of biologically-inspired polypeptides composed of repeat units of a Val-Pro-Gly-x-Gly motif, derived from the hydrophobic domain of topoelastin, with x representing any amino acid residue except proline [61]. ELPs exhibit the lowest critical solution temperature (LCST) behavior, meaning that they sensitively respond to temperature change: below a phase transition temperature, ELPs are soluble in water; above this temperature, they convert into an insoluble, polymer-rich, coacervate phase [61]. Leveraging the ability of ELPs to undergo highly reversible interconversion between these two phases in a temperature-sensitive manner, a specific ELP variant was utilized as the temperature sensing domain in ELP-TEMP [21].

Orange carotenoid protein (OCP) is a photoprotective carotenoid protein from cyanobacteria, comprising the N terminal domain (NTD) and the C terminal domain (CTD), which are connected by a long flexible loop linker [19]. It also contains the ketocarotenoid, 3′-hydroxyechinenone. In the dark and under low irradiance, OCP displays an orange color in its compact conformation, referred to as OCP^O. Upon intense irradiation with blue-green light, OCP transitions to an extended conformation, OCP^R, which is characterized by red color. Upon deactivation of the blue-green light, OCP^R reverts to OCP^O through a transition characterized by a rate constant that is temperature-dependent. In GETIs of TagRFP-OCP and OCP-TagGFP, the monitoring of the conformation change kinetics was devised through FRET, allowing for the estimation of temperature [19].

Fluorescence signals measured from GETIs

In measurement or imaging using a GETI, the fluorescence signal contains information on the sample's temperature, which is determined using a fluorescence signal-temperature standard curve (Figure 1). In this section, we explain what fluorescence signals are used in GETIs and how to measure them. Although some GETIs use only the fluorescence intensity from a single channel, this approach can sometimes pose challenges for temperature estimation, as discussed below (see **Single-band fluorescence intensity**). Instead, recent developments have focused on GETIs with fluorescence signals that are easier to interpret and apply for accurate temperature measurements. By definition, a "single-band" fluorescence signal originates from a single emission band with excitation at a single absorption band (Figure 4). Meanwhile, a "dual-band" fluorescence signal originates either from two emission bands with excitation at a single absorption band or from a single emission band with excitation at two absorption bands (Figure 4).

Single-band fluorescence intensity

Fluorescence intensity measures the number of photons that were emitted from a fluorescent object and reach a photosensor per unit time, making it a key observable in fluorescence measurements and imaging. It can be measured by a fluorescence spectrophotometer or a camera on a fluorescence microscope in a straightforward manner. However, fluorescence intensity is an extensive quantity, dependent on the size or scale of the system, such as the concentration of

the fluorescent molecule and the volume covered by a single sensor element (e.g., a pixel in a camera). Furthermore, in fluorescence spectroscopy measurements, fluorescence intensity depends on various factors, including the power density of excitation light, slit sizes for excitation and emission, the F-number of the spectroscope, integration time, sensor gain, and cuvette size. Similarly, fluorescence imaging of cells depends on various factors, including excitation light's power density, microscope optics' transmittance, the microscope objective's numerical aperture, camera gain, GETI's inhomogeneous distribution, cell thickness, and GETI diffusion. Accordingly, using single-channel fluorescence intensity known as the single-band intensiometry, or simply intensiometry, for purposes such as temperature estimation can be challenging. To circumvent this problem, in spectroscopy measurements using a cuvette, for example, one can accurately measure the fluorescence intensities of both a sample and a calibration standard under well-defined conditions, such as constant temperature, uniform light exposure, and fixed concentration. In fluorescence imaging of GETIs in cells, controlling measurement conditions can be more challenging. However, Kamei et al. previously demonstrated temperature imaging using intensiometry: they measured the fluorescence intensities of GFP in bacteria before and during heating with a NIR laser beam [12]. The initial intensity served as a reference, and the temperature during heating was estimated by comparing the fluorescence intensity during heating to that before heating. Especially in the context of fluorescence imaging of biological samples, fluorescence signals that are intensive quantity, meaning that ones independent of the system's extent, are preferably used as explained below.

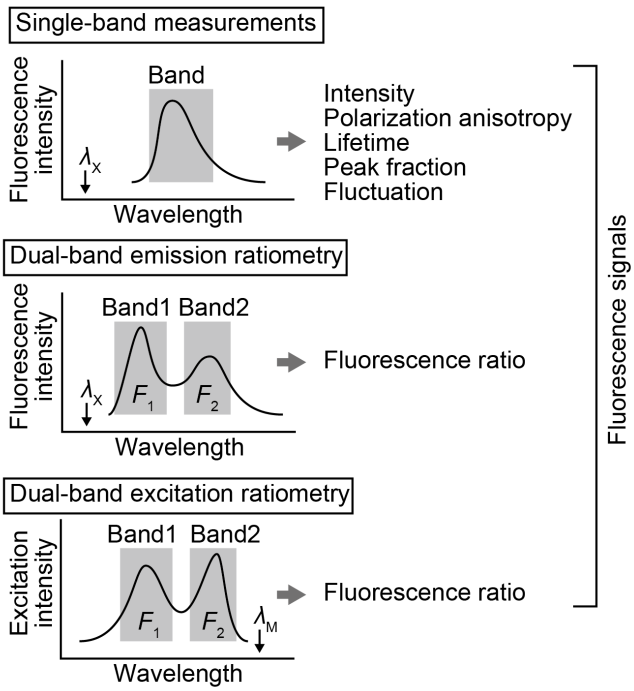

Figure 4 Schematic illustrations of single-band and dual-band fluorescence measurements to extract the fluorescence signals.

Dual-band fluorescence ratio

Dual-band fluorescence ratiometry, also known as fluorescence λ-ratiometry [66], or simply, fluorescence ratiometry, is a method for estimating a quantity of interest by using a ratio of fluorescence intensities measured at two different wavelengths. Because the nature of the extensive quantity for fluorescence intensity is canceled out by the calculation, appropriate fluorescence ratios can be handled as an intensive quantity. The dual-band fluorescence ratiometry calculates a rational function R, using two fluorescence intensities measured at two different wavelengths, for example,

$$R = \frac{F_1}{F_2}\ , \tag{7}$$

$$R = \frac{F_1}{F_1 + F_2}\ , \tag{8}$$

and so on, where F_1 and F_2 are fluorescence intensities measured from channels 1 and 2, respectively. The fluorescence intensities F_1 and F_2 can be emission intensities measured at two different wavelengths with the same excitation wavelength, corresponding to dual-band emission ratiometry. Alternatively, F_1 and F_2 can be emission intensities measured at the same wavelength but with excitation at two different wavelengths, corresponding to dual-band excitation ratiometry. In fluorescence spectroscopy, F_1 and F_2 can be easily obtained from the emission or excitation spectra for emission or excitation ratiometry (Figure 4). In contrast, when using a fluorescence microscope for fluorescence imaging, the measurement procedures between emission and excitation ratiometry differ significantly, due to varied techniques required to accurately capture and analyze the fluorescence signal.

In emission ratiometry fluorescence imaging, a fluorescence ratio image is computed from two raw images captured at

different emission wavelengths within the same field of view. Because the raw images are expected to reflect the quantity of interest at the same position and time, ideally, these raw images should be captured simultaneously. In this point of view, a convenient method to acquire two raw images is using dual-view optics, which splits a microscope-formed fluorescence image into two images at different emission wavelengths [67]. While laboratories can construct their own dual-view optics, commercially available versatile products, such as W-VIEW by Hamamatsu, Japan, are also available. A notable feature of using dual-view optics is that it allows for the capture of raw fluorescence images at two emission wavelengths simultaneously, without requiring any mechanical adjustments to the microscope components. Thus, the dual-view optics are particularly useful for emission ratiometric imaging at relatively fast frame rates (>1 frame/s). It should be noted that to achieve optimal results with dual-view optics, the use of high-quality dichroic mirror (e.g., those suitable for image splitting or super-resolution imaging) and bandpass filters is preferrable, and the optical alignment of the dual view optics must be carefully adjusted. Alternatively, emission ratiometric imaging can also be achieved by sequentially capturing fluorescence images at different emission wavelengths. This method involves using a motorized filter wheel installed between the microscope body and the camera, or a motorized filter turret within the microscope body, synchronized with the camera acquisition.

In excitation ratiometry, a fluorescence ratio image is computed from two raw images captured at the same emission wavelength but with two different excitation wavelengths. Unlike emission ratiometry, capturing raw fluorescence images at different excitation wavelengths simultaneously requires specific technical solutions in excitation ratiometry. Thus, in excitation ratiometry, raw fluorescence images are typically captured by alternately switching between excitation light sources by using a combination of light-emitting diodes (LEDs) or lasers equipped with digital modulation. For LEDs, examples include LightEngine Spectra X by Lumencor (Beaverton, OR, USA), Niji by BlueBox Optics (Blackwood, UK), and LedHUB by Omicron-Laserage Laserprodukte GmbH (Rodgau-Dudenhofen, Germany). About lasers, various wavelengths of solid-state lasers with digital and analogue modulation are now available. Previously, tsGFP, a GETI featuring excitation bands at 400 nm and 480 nm, was used for temperature imaging using dual-band excitation ratiometry [15].

Single-band fluorescence polarization anisotropy

When a sample containing fluorescent molecules is irradiated with linearly-polarized excitation light, fluorescence depolarization often occurs, which is quantified by the fluorescence polarization anisotropy (see **Fluorescence depolarization and rotational Brownian motion**). Since the steady-state fluorescence polarization anisotropy r (Equation (4)) represents a type of fluorescence ratio, it is also considered an intensive quantity. The steady-state fluorescence polarization anisotropy is determined by two mutually-orthogonal polarization components of fluorescence, parallel and orthogonal to the polarization of the continuous excitation light, as illustrated in Equation (4) and Figure 3B.

Many general-purpose fluorescence spectrophotometers are capable of being modified to measure steady-state fluorescence polarization anisotropy. In commonly-used L-format spectrophotometers as detailed by Lakowicz [41], polarizers for measuring fluorescence polarization anisotropy are typically available from the manufacturers and are installed in both the excitation and emission light paths. The two orthogonal polarization components of fluorescence are measured sequentially by adjusting the angle of the emission polarizer, allowing for the alternate capture of each component. Since the L-format entails mechanical adjustment of the polarizer, it is primarily suited for steady-state measurement. For kinetic analyses that require higher time resolution, such as those under 1 second, spectrophotometers designed specifically for rapid kinetic measurements are recommended.

Fluorescence polarization anisotropy imaging presents unique challenges not evident in cuvette-based fluorescence spectrophotometry, as noted by Axelrod [68]. Within a fluorescence microscope, the use of an objective with a high numerical aperture, covering a wide cone angle of light ray, can lead to significant rotation of the polarization in the collected fluorescence [68,69]. Additionally, fluorescence polarization can be altered by birefringence, which arises from the differential transmission of p- and s-polarization components at steep optical interfaces, such as those found in lenses and dichroic mirrors [69,70]. Consequently, as Axelrod observed, the measured value of fluorescence polarization anisotropy using a fluorescence microscope is often closer to zero than their true value due to these optical effects [68]. However, in certain cases, corrections can be applied to estimate a more accurate fluorescence polarization anisotropy value according to Axelrod's theoretical framework [68,71]. As an alternative method, we previously sought to correct the distorted fluorescence polarization using a $\lambda/4$ waveplate and an analyzer made from photonic crystal within a custom-built fluorescence microscope [69]. However, it is important to note that these photonic crystals required custom fabrication to match specific microscope objectives and dichroic mirrors. Furthermore, it is worth noting that in an inverted microscope, the polarization quality of light delivered from the side port is compromised due to an internal reflective element. As a solution, certain inverted microscopes offer a bottom port that delivers light with undisturbed polarization, circumventing the issue presented by the side ports.

Managing the polarization of excitation light in a fluorescence microscope is essential, though it is often simpler than controlling fluorescence polarization. Similar to fluorescence, the polarization of excitation light undergoes rotation when

passing through a microscope objective due to optical interactions. However, polarization can be significantly improved by meticulously designing and adjusting the optical configuration to ensure that the excitation light is highly collimated and equipped with a high-quality polarizer. Additionally, it is important to recognize that optical elements such as mirrors, prisms, and dichroic mirrors can significantly degrade light's polarization unless the light is precisely aligned as s- or p-polarized.

Single-band fluorescence lifetime

When a fluorescent molecule absorbs excitation light, it becomes excited and then returns to its ground state through a process called deactivation (Figure 2). The process of deactivation occurs over a time constant of the order of nanoseconds (~ns), known as the fluorescence lifetime. It is important to understand that the fluorescence lifetime is defined as $1/(k_r + k_{nr})$, not merely $1/k_r$, where k_r and k_{nr} represent the rate constants for radiative and nonradiative transitions, respectively, from the excited state back to the ground state (Equation (3), **Thermal fluorescence quenching**). Given that the fluorescence lifetime is an intensive quantity, it serves as a valuable parameter for estimating temperature. In this case, the fluorescence lifetime can be correlated with the thermal quenching (see **Thermal fluorescence quenching**) or a mechanism involving FRET and the temperature-dependent change of protein conformation or protein-protein interaction (see **Protein-protein interaction and conformation change**). Fluorescence lifetime can be measured using techniques such as time-correlated single photon counting (TCSPC) and phase modulation, also known as frequency domain fluorometry [41]. Frequency domain fluorometry employs excitation light modulated at MHz to GHz frequencies, analyzing the sample's fluorescence modulation amplitude and phase to ascertain lifetime parameters. TCSPC records the temporal decay of fluorescence intensity following excitation by short light pulses, with raw data subsequently analyzed in the time domain. With the commercial availability of state-of-the-art fast-response electronics and picosesond (ps) and femtosecond (fs) pulse lasers, TCSPC has become a widely utilized method for measuring fluorescence lifetime. Manufactures such as Pico-Quant (Berlin, Germany), Horiba Scientific (Kyoto, Japan), ISS (Champaign, IL, USA), Leica Microsystems (Wetzlar, Germany), and Becker & Hickl (Berlin, Germany) offer systems for fluorescence lifetime spectroscopy and microscopy. In a recent study, Silva et al. demonstrated a clear correlation between the fluorescence lifetime and temperature by using a fusion protein of actin and GFP (actin-GFP) expressed in HeLa cells [20].

Other fluorescence signals

Beyond the previously described fluorescence signals, additional signals from GETIs have been utilized for estimating temperature.

Fluorescence peak fraction. The emission spectrum of GFP shifts to longer wavelengths as temperature increases. Utilizing the fluorescence peak fraction technique, a spectrophotometer attached to a confocal microscope divides the GFP emission spectrum into two distinct wavelength regions to measure the intensities I_1 and I_2. The peak fraction, calculated as $(I_2 - I_1)/(I_2 + I_1)$, serves as a temperature indicator [18]. The method leverages the peak fraction as a direct measure of temperature variations.

Fluorescence fluctuation. A study reported that EGFP undergoes an acid-induced transition from a bright fluorescent state to a non-fluorescent dark state, characterized by a pK_a of approximately 6.0 [72]. This indicates that EGFP dynamically fluctuates between its bright and dark states under acidic conditions. The dynamic interconversion between these states was expected to result in observable fluorescence fluctuation, also known as blinking. Fluorescence correlation spectroscopy was used to measure the relaxation time of EGFP's fluorescence blinking, revealing a temperature dependence [11]. Accordingly, this led to the proposal of a novel molecular thermometer utilizing fluorescence blinking as its functional principle.

Rate constants and relaxation times of protein transitions. Many molecular processes' temperature dependence is explained through theories including the Arrhenius, Eyring, and Kramers equations [73]. In GETIs, if a molecular process triggers a temperature-dependent change in fluorescence signal, the process's rate constant or relaxation time serves as a reliable temperature indicator. Maksimov et al. created fusion proteins, OCP-TagGFP and TagRFP-OCP, by combining orange carotenoid protein, OCP, with TagGFP and TagRFP, respectively. These proteins demonstrated temperature-dependent fluorescence intensity relaxation, leading the authors to propose their potential as temperature indicators [19]. Furthermore, certain GFP-like proteins exhibit reversible photoswitching-fluctuating between bright and dark states, which hints at their potential for temperature sensing (see **GFP-like proteins**) [74]. The rate of photoswitching's correlation with temperature could serve as a foundational temperature sensing mechanism in future GETIs, with rate constants or relaxation times determined through fluorescence intensity's time trajectory analysis.

Development of GETIs

Design of GETIs

GETIs, being expressed from the cellular genes, are fundamentally designed based on gene expression mechanism,

utilizing gene engineering techniques to incorporate genes of FPs and various other proteins or polypeptides. From a structural design perspective, GETIs are categorized into two types: Type 1 involves either a sole FP or one fused with a localization-targeted protein or a polypeptide, whereas Type 2 consists of either two FPs or a combination of one or two FPs with temperature-responsive protein or polypeptide. Type 1 GETIs generate fluorescence signal from a single band, encompassing metrics like intensity, polarization anisotropy, lifetime, fluctuation, and peak fraction. Conversely, Type 2 GETIs are intricately designed to enhance temperature sensitivity and produce more controllable signals, such as dual-band fluorescence ratio. Previously-reported GETIs have primarily utilized conventional proteins and polypeptides as their foundational building blocks. Notably, there appears to have been a lack of attempts to enhance these building blocks through advanced protein engineering techniques, presenting an opportunity for future innovation. In addition, we note that FPs included in GETIs published to date are GFP-like proteins (Table 1).

GFP-like proteins

GFP-like proteins have become widely-utilized as probes for fluorescence bioimaging and as the building blocks in various genetically-encoded fluorescent indicators [5]. Currently, numerous GFP-like proteins have been identified and cloned from various organisms, with others being derived through protein engineering. For a comprehensive and current list of GFP-like proteins, refer to the FPbase website (https://www.fpbase.org/). GFP-like proteins feature an 11-stranded β-barrel structure, known as the "β-can", encapsulating a chromophore, typically 4-(p-hydroxybenzylidene)-5-imidazolinone) (p-HBI) or its derivative, autocatalytically generated from a tripeptide motif [42]. Within a GETI, GFP-like proteins serve versatile roles: they can function as a source of fluorescence emission, donor or acceptor in FRET, transducer of conformation changes, or temperature sensing domain. This is achieved through various processes including fluorescence thermal quenching, polarization anisotropy, fluctuation, lifetime, and peak fraction as detailed in the previous sections. It is important to recognize that GFP-like proteins possess characteristics that may either benefit or hinder the development of GETIs and their use in temperature measurement. Therefore, both developers and users must understand the properties of the GFP-like proteins in their GETIs, meticulously manage experimental condition, and thoroughly verify control experiments. We describe some important properties of GFP-like proteins as below.

pH dependence. Most GFP-like proteins maintain their folded, fluorescent conformation across pH levels 4–10, but become unfolded and non-fluorescent at extremely low and high pH values. Furthermore, the chromophore's ionization, specifically the dissociation of a proton (H^+) from its ionizable phenolic group, plays a crucial role in GFP-like proteins [42]. Differences in photoproperties, including absorption spectrum and fluorescence quantum yield between the ionized and deionized states of the chromophore, mean that pH shifts altering the chromophore's ionization can introduce noise to the fluorescence signal [42]. Thus, in temperature measurement, it is preferable for the chromophore's phenolic group pK_a in a GETI to be well outside the pH range of the sample. While tyrosine residues typically have an average pK_a of approximately 10.5 across various proteins [75], the β-can's chromophore phenolic group displays a wide range of pK_a values (~3–11), reflecting its involvement in a complex network of hydrogen bonding and other interactions.

Chromophore maturation. Following translation and folding, GFP-like proteins undergo chromophore maturation, a process where a tripeptide motif, typically Thr-Tyr-Gly, Met-Tyr-Gly, Ser-Tyr-Gly, or Cys-Tyr-Gly, is transformed into a fluorescent chromophore through cyclization, dehydration, and oxidation reactions [42]. Given that chromophore maturation occurs over minutes to hours, experiments should allow ample-time post-transfection with a GETI gene before beginning observations. In fact, if chromophore maturation in a GETI is insufficient, the experimenter may encounter diminished fluorescence intensity, reduced temperature sensitivity, and, in the case of indicators involving FRET, reduced FRET efficiency. For example, with B-gTEMP [22], we usually allow cells to be cultured for about 48 hours post-transfection with the B-gTEMP gene before conducting observation. Alternatively, establishing a stable cell line that expresses a GETI can mitigate the uncertainty associated with chromophore maturation.

Photobleaching. Photobleaching refers to the irreversible loss of fluorescence intensity under excitation light irradiation, affecting both ensembles of fluorescent molecules and individual molecules. Photobleaching in GFP-like proteins is attributed to the irreversible damage to the chromophore's π-electron system and oxidation of adjacent amino acids [76,77]. It is crucial to address photobleaching, particularly during long term observation or when using high illumination power density, to maintain fluorescence signal integrity. As a solution to photobleaching, the recently developed GFP-like protein, StayGold, has shown significantly enhanced photostability compared to traditional GFP-like proteins [78], presumably offering promising prospects for future GETI development.

Photoactivation and photoconversion. Certain GFP-like proteins can irreversibly transition from a non-fluorescent (dark) state to a fluorescent (bright) state when exposed to light of a specific wavelength, termed photoactivatable FPs [74]. Additionally, some other GFP-like proteins can irreversibly change their fluorescence from one color to another under specific wavelength light irradiation, identified as photoconvertible FPs [74]. The photoactivation and photoconversion processes are believed to involve the photo-cleavage of amino acid residues or the polypeptide backbone near the chromophore [42], making these processes valuable for developing genetically-encoded fluorescent indicators. For instance, CaMPARI is a photoconvertible genetically-encoded Ca^{2+} indicator that shifts its fluorescence from green

to red upon Ca^{2+} binding and violet light exposure [79]. The irreversibility of photoconversion not only made CaMPARI an effective tool for capturing Ca^{2+} activity, but also suggests that similar mechanisms could advance future GETI development.

Reversible photoswitching. Several GFP-like proteins can reversibly switch between dark (off) and bright (on) states upon exposure to lights of specific wavelengths, classified as reversibly photoswitchable fluorescent proteins (RSFPs). Transition from the on state to the off state and vice versa are termed off and on switching, respectively. RSFPs' reversible photoswitching is believed to be driven by photo-induced cis-trans isomerization or chromophore hydration/dehydration processes [42,80]. The rate constants for the on and off switching are independent of RSFP concentration, although they are influenced by the irradiation light's power density. Furthermore, rational functions based on the asymptotic fluorescence intensities during on and off switching, such as the on/off contrast, are determined by the photoswitching rate constants, and are also independent of protein concentration, making them valuable fluorescence signals for measurement. Previously, a reversibly photoswitchable genetically-encoded Ca^{2+} indicator CaMP6s-Q was reported, utilizing photoswitching contrast $(F_0 - F_{end})/F_0$ as a quantitative measure of $[Ca^{2+}]$, where F_0 and F_{end}, respectively, represent the initial and asymptotic fluorescence intensities during off switching measured under a constant power density of irradiation lights for photoswiching [81]. It should be noted that the photoswitching kinetics of certain RSFPs are also influenced by factors like pH and solvent viscosity, highlighting the need for caution due to potential crosstalk [82,83].

Linkers

Fusion proteins, consisting of multiple domains, often include linkers connecting two domains to optimize distance, orientation, and rotational dynamics between the domains while preventing their interference. Linkers in fusion proteins are classified as short, flexible, semiflexible, structured, and random [84]. For example, $(Gly\text{-}Gly\text{-}Ser)_n$ represents a typical flexible linker, while $(Glu\text{-}Ala\text{-}Ala\text{-}Ala\text{-}Lys)_n$ exemplifies a structured linker [84,85]. To date, fine tuning of linkers in a GETI remains largely explored. Given the critical roles of linkers in optimizing FRET between two FPs and facilitating the transmission of conformational change, the refinement of linkers between domains is likely to spur further development of GETIs.

Protein engineering

While conventionally-known proteins and polypeptides have been the building blocks for existing GETIs, future developments may benefit significantly from advanced protein engineering techniques. Rational design methods, including site-directed mutagenesis and site-specific sequence insertions and deletions, play a crucial role in protein improvement based on structural insights. However, directed evolution involving gene diversification and variant screening cycles has become a staple approach in protein engineering [86]. For example, directed evolution has led to the development of numerous GFP-like proteins including Kohinoor, Gamillus, and Kohinoor 2.0 as demonstrated in our recent studies [87,72,82]. This section provides a concise overview of key directed evolution techniques pivotal to advancing GFP-like protein engineering.

Random mutagenesis, which introduces mutations at nonspecific sites, is instrumental in generating protein libraries, especially when the structure-function relationship is unclear. Error-prone PCR, a technique for random mutagenesis, amplifies DNA with high concentrations of Mg^{2+} and Mn^{2+} along with imbalanced concentrations of dATP, dCTP, dGTP, and dTTP, thereby introducing random mutations [88]. Moreover, transposon-based mutagenesis approach called TRIAD has been utilized to create libraries of random variants featuring short in-frame insertions and deletions [89]. With available structure information of a protein, site-saturation mutagenesis enables the creation of libraries with all possible mutations at targeted sites [90].

Variant libraries can be generated through the combinatorial mixing of DNA fragments from a library or by combining multiple DNA sequences with high homology. DNA shuffling, a DNA recombination technique, involves creating a library by random fragmenting homologous DNAs with DNase I, followed by reconstituting full-length DNAs via self-priming PCR [91]. The StEP (Staggered Expansion Process), another DNA recombination method for generating variant libraries, uniquely operates without DNase I. This relies on repeated cycles of thermal denaturation, brief annealing, and elongation by DNA polymerase to reconstitute full-length DNAs [92].

Circular permutation involves rearranging a protein's structure to connect its original N- and C-terminals, typically via a polypeptide linker, creating new N- and C-terminals at a different sequence position [93]. When fusing two FPs, circular permutation is useful to change their relative orientation, thereby affecting FRET's orientation factor. For example, circular permutation was proved to be valuable in optimizing FRET efficiency between two FPs in FRET-based Ca^{2+} indicators [94]. Furthermore, circular permutation of GFP-like proteins has facilitated the development of various genetically-encoded fluorescent indicators, creating new N- and C-terminals near the chromophore to fuse with sensing domains [95].

To screen for variants, genes from a DNA library are expressed in a specific cell type for subsequent assays. *E. coli* cells are commonly used for screening GFP-like protein variants, because each colony on a solid medium originates from a

single clone. This allows for the easy testing of fluorescence properties via light irradiation and straightforward picking of individual clones. Conversely, certain proteins, such as G protein-coupled receptors, are exclusively expressed in eukaryotic cells [96]. Similarly, genetically-encoded indicators that contain protein kinase A were reported not to function in *E. coli* cells [97]. Therefore, for screening these variants, they should be expressed in suitable types of cells such as yeast cells and mammalian cells. Furthermore, while the throughput for screening variants in mammalian cells is typically limited, a microscopy-guided robotic cell-picking strategy was reported to address this issue [98]. As a result, there is considerable potential for significantly enhancing the throughput of library screening in mammalian cells in future.

Monitoring appropriate properties of FP variants for the screening of a library is also crucial. In the screening of FP libraries, using *E. coli* as the expression system, properties such as fluorescence intensity, emission wavelength, and photochromism are often evaluated. For example, our laboratory utilizes an in-house built monitoring system to expose *E. coli* colonies expressing FP variants on a petri dish to excitation and photoswitching lights, capturing images through a bandpass filter using a CCD camera. Additionally, screening based on fluorescence lifetime has recently been reported [99–101], and thus, screening by fluorescence lifetime is likely to be also instrumental in developing GETIs based on the thermal quenching mechanism.

GETIs

In this section, we briefly introduce some representative GETIs, and we encourage interested readers to consult the original papers for detailed information. In addition, most GETIs' genes can be accessed through plasmid depositories such as Addgene (https://www.addgene.org/).

GFP and EGFP

GFP, its variants, and their simple fusions with proteins or signal polypeptides for specific localization, have found diverse applications in temperature measurement and imaging. Kamei et al. utilized EGFP's temperature dependent fluorescence intensity for intensiometric temperature measurements in *E. coli* [12]. Donner et al. employed GFP and glutamic decarboxylase-fused GFP for fluorescence polarization anisotropy imaging of heating-induced temperature changes in HeLa and U-87 MG cancer cells, and *C. elegans* [13,14]. Furthermore, Kaur et al. explored GFP's fluorescence polarization anisotropy alongside the impacts of temperature and high pressure [102]. Savchuk et al. developed peak fraction analysis to identify GFP's spectral shift enabling temperature and thermogenesis imaging in HeLa cells' mitochondria [18]. Silva et al. conducted temperature imaging with actin-GFP expressed in HeLa cells, using fluorescence lifetime during hyperthermia treatment under an alternating magnetic field [20]. Moreover, Wong et al. introduced a method for measuring temperature via the fluorescence blinking of EGFP, as detected by fluorescence correlation spectroscopy [11].

GFP-TlpA and tsGFP

The thermo-responsive protein TlpA, identified in Salmonella typhimurium [60] (see **Protein-protein interaction and conformation change**), served as the basis for GETIs GFP-TlpA and tsGFP [10,15]. GFP-TlpA, a fusion of GFP and TlpA (Figure 5), represents one of the earliest GETIs created by fusing a GFP-like protein with a non-FP protein for temperature sensing. GFP-TlpA excited at 395 nm showed a fluorescence intensity increase with temperature, and it was tested as an intensiometric GETI with a temperature sensitivity $S_{F,T}$ = +0.82 %/°C (Table 1; for definition, see **Temperature sensitivity** (below)). TlpA undergoes a structural transition from a coiled-coil dimer at low temperatures to a random coil monomer at high temperatures [10,63]. This change likely influences the GFP domain's conformation, causing a shift in the equilibrium between the ionized and deionized states of the GFP chromophore's phenolic group and thus altering the absorbance around 400 nm. GFP-TlpA underwent testing in an aqueous buffer solution [10].

tsGFP, another fusion protein combining GFP and TlpA, uniquely features GFP inserted between a tandem repeat of two TlpA polypeptides (Figure 5) [15]. The researchers engineered two variants of tsGFPs: tsGFP1, featuring a truncated TlpA (94–257), and tsGFP2, incorporating the full-length TlpA (1–371) (Figure 5). tsGFPs have two excitation bands at 400 nm and 480 nm with fluorescence intensities at these wavelengths decreasing and increasing, respectively, as temperature rises. As a result, they are applicable as dual-band excitation ratiometric GETIs by calculating the fluorescence intensity ratio excited at 400 nm to that at 480 nm (R(ex400/ex480)). For both tsGFP1 and tsGFP2, the fluorescence ratio R(ex400/ex480) decreases with temperature, reaching critical temperature where temperature sensitivity $S_{R(ex400/ex480),T}$ becomes pronounced. The critical temperatures were determined as 37.6 °C for tsGFP1 and 42.3 °C for tsGFP2 with temperature sensitivities $S_{R(ex400/ex480),T}$ of −3.92 %/°C (34–41°C) and −3.82 %/°C (38–46°C), respectively. Similar to GFP-TlpA, the temperature-induced conformation change in TlpA is thought to influence GFP, shifting the pH-dependent equilibrium of the ionizable phenolic group in the chromophore and altering the absorption spectrum. tsGFP1 enabled precise imaging of thermogenesis within the mitochondria of HeLa cells and brown adipocytes as well as in the sarcoplasmic reticulum of myotubes [15].

gTEMP

gTEMP, which we developed, represents one of the earliest GETIs utilized for dual-band emission ratiometry [17]. The gTEMP gene contains DNA sequences for Sirius, the T2A polypeptide, and mT-Sapphire with the T2A amino acid sequence being Glu-Gly-Arg-Gly-Ser-Leu-Leu-Thr-Cys-Gly-Asp-Val-Glu-Glu-Asn-Pro-Gly-Pro (Figure 5) [103–105]. Upon cellular expression of gTEMP, the ribosomal skip mechanism [104] cleaves the Gly-Pro linkage at T2A's C-terminal, resulting in the separation of Sirius and mT-Sapphire, thereby, preventing FRET between Sirius and mT-Sapphire. When excited by near ultraviolet light (~360 nm), both GFP-like proteins, Sirius and mT-Sapphire, fluoresce with peak wavelengths at 424 nm and 511 nm, respectively, due to direct excitation. Despite both fluorescence emission bands undergoing thermal quenching, the Sirius band showed greater temperature sensitivity compared to the mT-Sapphire band. Consequently, the fluorescence intensity ratio of mT-Sapphire to Sirius served as an effective temperature measure. While examining a fusion protein of Sirius and mT-Sapphire, we found that gTEMP's temperature sensitivity, indicated by the fluorescence ratio $S_{R,T}$, surpassed that of the Sirius/mt-Sapphire fusion. Using gTEMP, we successfully detected temperature increase in mitochondria of HeLa cells following FCCP stimulation and mapped temperature distribution in an embryo of Japanese rice fish (*Orizias latipes*).

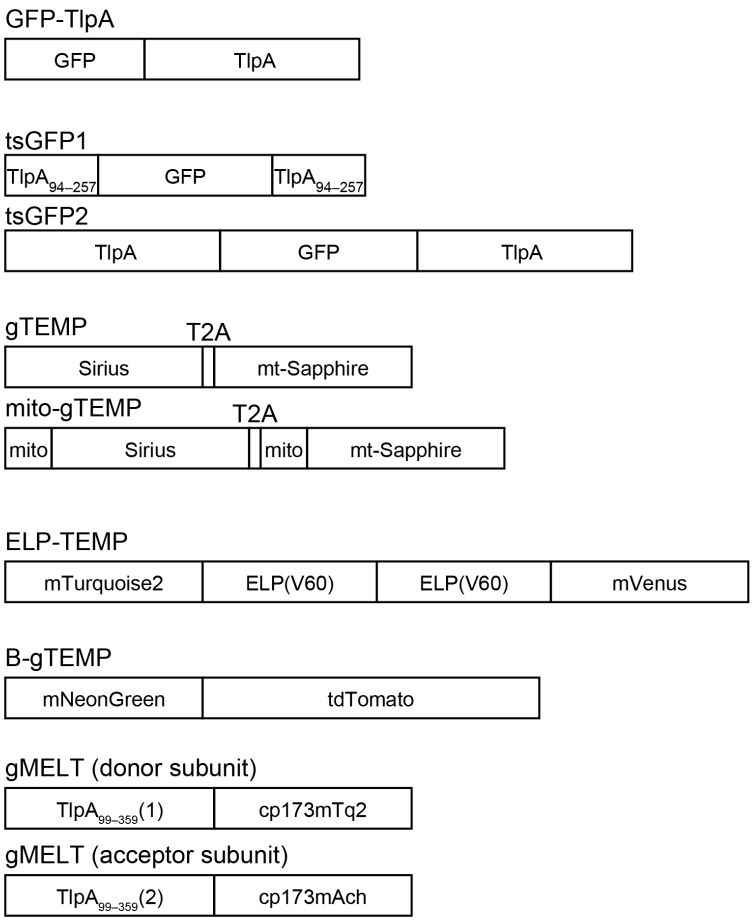

Figure 5 Schematic illustrations of DNA constructs of GFP-TlpA, tsGFP1, tsGFP2, gTEMP, mito-gTEMP, ELP-TEMP, B-gTEMP, and gMELT. mito, mitochondrial targeting sequence derived from the subunit-VIII precursor; TlpA, full-length TlpA protein; $TlpA_{94–257}$, coiled coil domain fragment from TlpA (residues 94–257); $TlpA_{99–359}$(1), coiled coil domain fragment from TlpA (residues 99–359) with two sets of mutations D135V/K187R/K202I/L208Q and E180R/E250R; $TlpA_{99–359}$(2), coiled coil domain fragment from TlpA (residues 99–359) with two sets of mutations D135V/K187R/K202I/L208Q and R179E/R251E; cp173mTq2, circularly permutated variant of mTurquioise2; cp173mAch, circularly permutated variant of mAchilles.

ELP-TEMP

ELP-TEMP represents another advanced GETI we developed, characterized by its high temperature sensitivity for the dual-band emission ratiometry [21]. Comprising mTurquoise2 [100] as the FRET donor, mVenus [106] as the FRET acceptor, and the temperature-responsive polypeptide ELP (see **Protein-protein interaction and conformation change**) [61], ELP-TEMP integrates these components for its function (Figure 5). ELP-TEMP transitions from a soluble dispersed state at low temperatures below 35 °C to a favored coacervate state above 35 °C, a process that is highly reversible and temperature-dependent. In low-temperature conditions, ELP-TEMP remains dispersed, with the ELP domain keeping mTurquoise2 and mVenus apart, resulting in reduced FRET efficiency. Upon reaching high temperature, ELP-TEMP undergoes self-assembly into coacervates, bringing mTurquoise2 and mVenus closer together and thereby significantly increasing FRET efficiency. The temperature-dependent FRET efficiency enables ELP-TEMP to facilitate dual-band emission ratiometry imaging using a single excitation wavelength for mTurquioise2 such as 445 nm. The pronounced temperature sensitivity observed in HeLa cells (maximum $S_{R,T}$, +44 %/°C in the nucleus and +19 %/°C in the cytoplasm) is attributed to the phase transition behavior of ELP [61]. While ELP-TEMP's temperature response can be affected by macromolecular crowding and self-concentration, we overcame these issues by creating a stable cell line expressing ELP-TEMP and conducting calibration under conditions that mimicked cellular environment. Utilizing ELP-TEMP, we were able to precisely detect temperature changes in HeLa cells triggered by ionomycin stimulation.

B-gTEMP

B-gTEMP is a fusion of two GFP-like proteins mNeonGreen and tdTomato (Figure 5) [47,107] that we developed [22], and it is designed as GETI for dual-band emission ratiometry with fast response to abrupt temperature changes. An earlier emission ratiometry GETI of gTEMP required near UV light (~360 nm) for excitation, but the phototoxicity to cells could be encountered. Thus, we tried to develop B-gTEMP to solve the phototoxicity. B-gTEMP is excited with a blue light (~480 nm) and the fluorescence bands of both mNeonGreen and tdTomato are observed. Although both fluorescence bands showed thermal quenching, tdTomato has a greater degree of quenching compared to mNeonGreen. Thus, the fluorescence intensity ratio of mNeonGreen to tdTomato was used as a measure of temperature. Being a fusion protein, the two fluorescent protein domains in B-gTEMP are bound, and the FRET efficiency between mNeonGreen to tdTomato was measured to be ~75%. However, the FRET efficiency was little dependent on temperature, and the temperature change of the FRET efficiency was estimated to contribute to the overall temperature sensitivity $S_{R,T}$ by <10% (see **The sensitivity analysis of dual-band emission ratiometric GETIs**). According to our analysis, 90% of the temperature sensitivity of B-gTEMP, $S_{R,T}$, was attributed to the thermal quenching of tdTomato. Furthermore, the temperature response of B-gTEMP exhibited minimal influence from macromolecular crowding. Together with the primary contribution of thermal quenching, it is probable that B-gTEMP undergoes little conformational change in response to temperature variations. This would be consistent with our observation of fast response of B-gTEMP fluorescence to an abrupt temperature leap with a time constant of < 1 ms. Leveraging B-gTEMP's rapid response, we conducted direct observation of heat diffusion within cells expressing B-gTEMP. Employing a carbon nanotube cluster irradiated by a focused red laser beam as a heat source enabled us to in real time track the heat diffusion process within cells.

gMELT

We recently developed gMELT, a dual-band emission ratiometry GETI with high temperature sensitivity and ability to specifically localize within cells [24]. gMELT is composed of donor and acceptor subunits containing cp173mTurquoise2, a variant of mTurquoise2 [99], and cp173mAchilles, a variant of mAchilles [108], which serve as the donor and acceptor of FRET, respectively, and are fused with engineered TlpA coiled-coil domains (Figure 5). We integrated two sets of mutations into the coiled-coil domain of TlpA (residues 99–359; $TlpA_{99–359}$) for the donor and acceptor subunits: one set of mutations, D135V/K187R/K202I/L208Q, was for optimizing the response temperature [64]; the other set of mutations, E180R/E250R (G2A3 mutation) for the donor subunit or R179E/R251E (G2B3 mutation) for the acceptor subunit, was aimed at promoting the heterodimerization of TlpA domains [65]. Accordingly, the donor subunit is a fusion of cp173mTurquoise2 and $TlpA_{99–359}$ with the mutations D135V/K187R/K202I/L208Q and E180R/E250R ($TlpA_{99–359}$(1) in Figure 5), and the acceptor subunit is a fusion of cp173mAchilles and $TlpA_{99–359}$ with the mutations D135V/K187R/K202I/L208Q and R179E/R251E ($TlpA_{99–359}$(2) in Figure 5). Similar to GFP-TlpA and tsGFP, the engineered $TlpA_{99–359}$ domains in the donor and acceptor subunits play a key role in the temperature response mechanism. At low temperatures (< 35 °C), gMELT forms a heterodimer composed of one donor subunit and one acceptor subunit through the engineered $TlpA_{99–359}$ domains due to the heterodimerization mutations, resulting in high FRET efficiency. Above 35 °C, the heterodimer state of gMELT undergoes subunit dissociation, resulting in the disappearance of FRET. Accordingly, gMELT can report temperature through the fluorescence ratio of cp173mTurquoise2 (cyan fluorescence) to cp173mAchilles (yellowish green fluorescence), and achieved remarkably high temperature sensitivities $S_{R,T}$ of +39.3 %/°C, +33.8 %/°C, and +22.0 %/°C at 34–36 °C in cytoplasm, endoplasmic reticulum (ER), and mitochondria of HeLa cells, respectively. We leveraged gMELT specifically targeting the ER and mitochondria (gMELT-ER and gMELT-

Mito, respectively) to visualize thermogenesis in these organelles of HeLa cells stimulated with FCCP. Additionally, we note that, unlike ELP-TEMP, gMELT does not form coacervates or aggregates, and gMELT-ER and gMELT-Mito were confirmed to exhibit correct localization in the organelles.

Evaluation of GETIs

When a GETI or a temperature measurement method using a GETI is developed, the developer needs to evaluate its performance and determine the appropriate measurement condition for use. In this section, we present the standards of evaluation procedures of GETIs.

Temperature sensitivity

The sensitivity of the fluorescence signal of a GETI to a temperature change is evaluated using the temperature sensitivity $S_{s,T}$ (the unit is K^{-1} or $°C^{-1}$, and, for presentation purpose, %/K or %/°C is often used in the literature) and the temperature coefficient Q_{10}, although $S_{s,T}$ seems more commonly used in GETI-related studies. These parameters are defined as

$$S_{s,T} = \frac{1}{s} \cdot \frac{\Delta s}{\Delta T} \ , \tag{9}$$

and

$$Q_{10} = \left[\frac{s(T_2)}{s(T_1)} \right]^{(T_2 - T_1)/10} \ , \tag{10}$$

where s is the fluorescence signal, T is the temperature, Δs is the change in s due to a temperature shift ΔT, and $s(T_1)$ and $s(T_2)$ are the fluorescence signals at temperatures T_1 (K) and T_2 (K) (Figure 6A). The quantities $S_{s,T}$ and Q_{10} are approximately related by the following equation:

$$Q_{10} \approx \exp\left(10 \cdot S_{s,T}\right) \ . \tag{11}$$

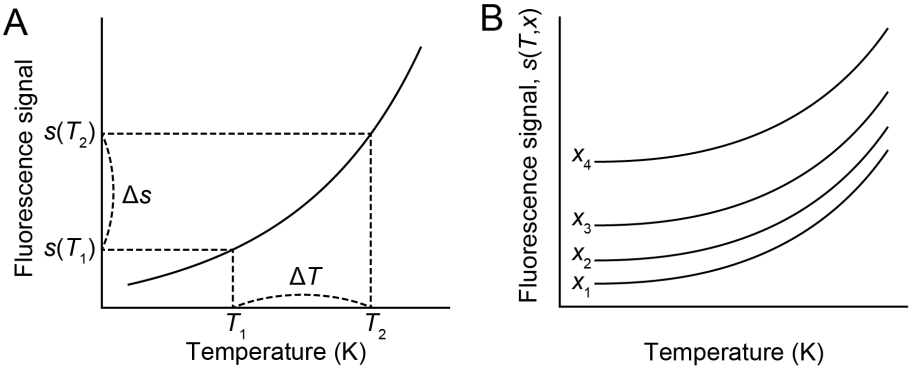

Figure 6 Schematic illustrations of temperature change of a fluorescence signal. (A) A schematic plot of fluorescence signal against temperature. (B) Schematic plots of fluorescence signal against temperature at several values of condition parameter x.

Temperature resolution

In thermal biology, temperature resolution, or temperature uncertainty, refers to how small temperature change or temperature difference can be resolved and is calculated as the deviation of the estimated temperature. Unfortunately, the definition of temperature resolution often varies between papers. It may refer to (1) the standard deviation of estimated temperatures across a number of cells (right top in Figure 7), (2) the standard deviation within a specific region of interest in a cell during time-lapse observations (bottom right in Figure 7), or (3) the standard error or deviation of data obtained

from a series of repeated fluorescence measurements in a cuvette. Thus, readers need to determine what a paper means by "temperature resolution" based on the context, and, more importantly, authors must clearly define their temperature resolution. In any case, the temperature resolution in a temperature measurement experiment using a GETI is related to the deviation of the fluorescence signal. Let $\sigma(s)$ represent the standard deviation or error of a fluorescence signal s, then the temperature resolution is calculated using the error propagation method as

$$\sigma(T)=\left|\frac{\Delta T}{\Delta s}\cdot\sigma(s)\right|=\left|\frac{1}{\frac{1}{s}\cdot\frac{\Delta s}{\Delta T}}\cdot\frac{\sigma(s)}{s}\right|=\left|\frac{1}{S_{s,T}}\cdot\frac{\sigma(s)}{s}\right|, \quad (12)$$

where $S_{s,T}$ is defined in Equation (9).

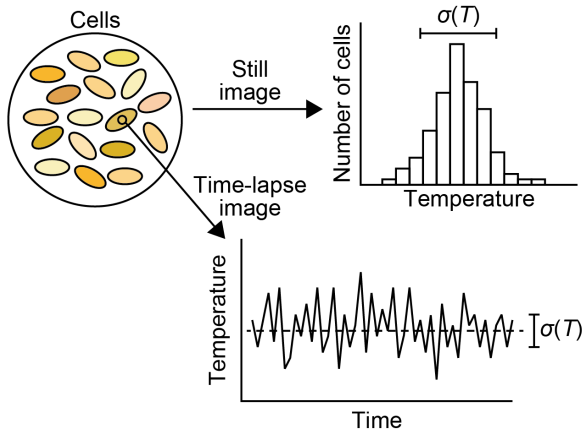

Figure 7 Two types of temperature resolution. (Top right) A temperature resolution reflecting the variation of estimated temperatures over cells under observation. (Bottom right) A temperature resolution reflecting the variation of estimated temperature in the time trajectory measured at a region in a cell.

The sensitivity analysis of dual-band emission ratiometric GETIs

In temperature measurements using a GETI with the dual-band emission ratiometry, the fluorescence intensities of the two emission bands are measured. For example, when we developed B-gTEMP, a dual-band emission ratiometric GETI, we analyzed how its photophysical properties affected the temperature sensitivity [22]. Specifically, we examined the effects of the extinction coefficients and fluorescence quantum yields of mNeonGreen and tdTomato, as well as the FRET efficiency between them. This analysis was performed based on the analytical form of a fluorescence ratio R, referred to as the FRET ratiometry formula, given by

$$R(1/2)=\frac{F_{1,\mathrm{obs}}}{F_{2,\mathrm{obs}}}=\frac{C_{\mathrm{D},1}}{C_{\mathrm{A},2}}\cdot\frac{\phi_{\mathrm{D}}(1-E)}{\phi_{\mathrm{A}}\left(E+\frac{\varepsilon_{\mathrm{A}}}{\varepsilon_{\mathrm{D}}}\right)}, \quad (13)$$

where the indexes D and A represent the donor FP and acceptor FP, respectively, the indexes 1 and 2 correspond to the detection channels for the fluorescence bands of D and A, respectively, and $F_{1,\mathrm{obs}}$ and $F_{2,\mathrm{obs}}$ are the readouts of the fluorescence intensities from channels 1 and 2, respectively (Figure 8). The variables ε_{D} and ε_{A} represent extinction coefficients for D and A, respectively, at the excitation wavelength of D (λ_x in Figure 8), ϕ_{D} and ϕ_{A} are the fluorescence quantum yields of D and A, respectively, and E is the FRET efficiency. Furthermore, $C_{i,j}$ represents the ratio of the observed fluorescence intensity through channel j (1 or 2) to the spectral integral intensity of FP i (D or A). This instrument constant $C_{i,j}$ depends on the spectral transmittance of a bandpass filter, the spectral quantum efficiency of a camera, and the fluorescence emission spectrum of FP i. Although we assumed that $C_{\mathrm{D},2}=C_{\mathrm{A},1}=0$ in Equation (13), the formula for non-zero $C_{\mathrm{D},2}$ and $C_{\mathrm{A},1}$ is also available in ref [22]. In addition, if a GETI of interest does not involve FRET, it suffices to assume that $E=0$ in Equation (13).

The analytical form of the temperature sensitivity $S_{R,T,\mathrm{anal}}$ (K^{-1}) is computed using the total differentiation given by

$$\begin{aligned}S_{R,T,\mathrm{Anal}}&=\frac{1}{R(1/2)}\cdot\frac{dR(1/2)}{dT}\\&=\frac{1}{R}\cdot\left[\left(\frac{\partial R}{\partial\phi_{\mathrm{D}}}\right)\frac{d\phi_{\mathrm{D}}}{dT}+\left(\frac{\partial R}{\partial\phi_{\mathrm{A}}}\right)\frac{d\phi_{\mathrm{A}}}{dT}+\left(\frac{\partial R}{\partial\varepsilon_{\mathrm{D}}}\right)\frac{d\varepsilon_{\mathrm{D}}}{dT}+\left(\frac{\partial R}{\partial\varepsilon_{\mathrm{A}}}\right)\frac{d\varepsilon_{\mathrm{A}}}{dT}+\left(\frac{\partial R}{\partial E}\right)\frac{dE}{dT}\right],\end{aligned} \quad (14)$$

where ε's, ϕ's, and E are taken as the independent variables in the total differentiation. Based on this equation, we can decompose the temperature sensitivity into components corresponding to of ε's, ϕ's, and E. To combine Equation (14) with experimental data, we replace d's to Δ's, yielding the temperature sensitivity components as follows:

$$S_{R,T}(\phi_{\mathrm{D}}) = \frac{1}{R}\cdot\left(\frac{\partial R}{\partial \phi_{\mathrm{D}}}\right)\cdot\frac{\Delta\phi_{\mathrm{D}}}{\Delta T} = \frac{1}{\phi_{\mathrm{D}}}\cdot\frac{\Delta\phi_{\mathrm{D}}}{\Delta T}\ , \tag{15}$$

$$S_{R,T}(\phi_{\mathrm{A}}) = \frac{1}{R}\cdot\left(\frac{\partial R}{\partial \phi_{\mathrm{A}}}\right)\cdot\frac{\Delta\phi_{\mathrm{A}}}{\Delta T} = -\frac{1}{\phi_{\mathrm{A}}}\cdot\frac{\Delta\phi_{\mathrm{A}}}{\Delta T}\ , \tag{16}$$

$$S_{R,T}(\varepsilon_{\mathrm{D}}) = \frac{1}{R}\cdot\left(\frac{\partial R}{\partial \varepsilon_{\mathrm{D}}}\right)\cdot\frac{\Delta\varepsilon_{\mathrm{D}}}{\Delta T} = \frac{1}{1+\frac{\varepsilon_{\mathrm{D}}}{\varepsilon_{\mathrm{A}}}E}\cdot\frac{1}{\varepsilon_{\mathrm{D}}}\cdot\frac{\Delta\varepsilon_{\mathrm{D}}}{\Delta T}\ , \tag{17}$$

$$S_{R,T}(\varepsilon_{\mathrm{A}}) = \frac{1}{R}\cdot\left(\frac{\partial R}{\partial \varepsilon_{\mathrm{A}}}\right)\cdot\frac{\Delta\varepsilon_{\mathrm{A}}}{\Delta T} = -\frac{1}{1+\frac{\varepsilon_{\mathrm{D}}}{\varepsilon_{\mathrm{A}}}E}\cdot\frac{1}{\varepsilon_{\mathrm{A}}}\cdot\frac{\Delta\varepsilon_{\mathrm{A}}}{\Delta T}\ , \tag{18}$$

and,

$$S_{R,T}(E) = \frac{1}{R}\cdot\left(\frac{\partial R}{\partial E}\right)\cdot\frac{\Delta E}{\Delta T} = -\frac{1+\frac{\varepsilon_{\mathrm{D}}}{\varepsilon_{\mathrm{A}}}}{(1-E)\left(1+\frac{\varepsilon_{\mathrm{D}}}{\varepsilon_{\mathrm{A}}}E\right)}\cdot\frac{\Delta E}{\Delta T}\ . \tag{19}$$

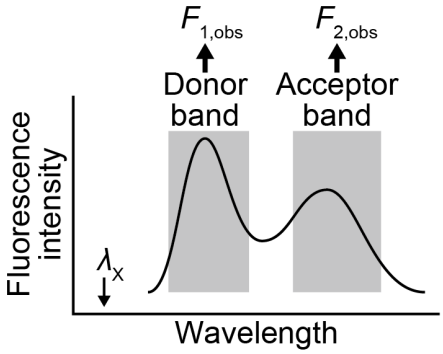

Figure 8 Measurement of a dual-band emission ratiometric GETI undergoing FRET. The donor and acceptor bands are measured through channels 1 and 2 to take fluorescence intensities $F_{1,\mathrm{obs}}$ and $F_{2,\mathrm{obs}}$, respectively.

It should be noted that the temperature changes of ε's and ϕ's, for D and A, as well as the FRET efficiency E, can be experimentally measured. Therefore, these temperature sensitivity components can be evaluated. In the analysis of B-gTEMP using this procedure, we found that its temperature sensitivity is primarily attributed to the temperature-dependent change in the fluorescence quantum yield of tdTomato. Therefore, we concluded that the primary mechanism of temperature sensitivity was thermal quenching [22].

Additionally, the second fraction on the right-hand side of Equation (13) can be explained qualitatively. Suppose that excitation light is incident on a GETI molecule. The probability of donor D excitation without quenching by FRET is proportional to $(1 - E)$. Therefore, the fluorescence intensity of D should be proportional to $\phi_{\mathrm{D}}(1 - E)$, which corresponds to the numerator in Equation (13). The probability of A excitation due to FRET is proportional to E, while the probability of the direct excitation of A relative to that of D is proportional to $\varepsilon_{\mathrm{A}}/\varepsilon_{\mathrm{D}}$. Thus, the fluorescence intensity of A should be proportional to $\phi_{\mathrm{A}}(E + \varepsilon_{\mathrm{A}}/\varepsilon_{\mathrm{D}})$, which corresponds to the denominator in Equation (13). In addition, the FRET efficiency E is known to depend on the donor fluorescence quantum yield ϕ_{D} and the acceptor extinction coefficient ε_{A} [41]. However, for the partial derivative $(\partial R/\partial E)$, ϕ_{D} and ε_{A} are considered operationally fixed, and the effects of the temperature-induced changes in ϕ_{D} and ε_{A} on E are included in the measured data of ΔE.

Crosstalk in temperature measurement with GETIs

Because FPs and temperature-sensitive polypeptides can be affected not only by temperature but also by other factors, it is necessary to examine how specifically a GETI responds to temperature changes. These factors include pH, ions, macromolecular crowding, specific ligands, the self-concentration of GETI, and photophysical as well as photochemical reactions. We also tested these factors during the development of our recent GETIs [17,21,22,24].

If an effect of a condition parameter x (e.g., ion concentration) on the fluorescence signal s of a GETI is observed (Figure 6B), we may then be interested in how much the estimated temperature T_{e} is influenced by the deviation of s. This relationship can be analyzed quantitatively. Suppose that a change in the condition parameter, Δx, gives rise to a change in the fluorescence signal, Δs. Then, the deviation of the estimated temperature ΔT_{e} due to such a condition change is calculated using the chain rule in calculus as

$$\Delta T_{\mathrm{e}} = \frac{\Delta T}{\Delta s}\cdot\frac{\Delta s}{\Delta x}\cdot\Delta x = \frac{1}{\frac{1}{s}\cdot\frac{\Delta s}{\Delta T}}\cdot\frac{1}{s}\cdot\frac{\Delta s}{\Delta x}\cdot\Delta x = \frac{S_{x,s}}{S_{s,T}}\cdot\Delta x\ , \tag{20}$$

where $S_{x,s}$ represents the sensitivity of the fluorescence signal s to the condition parameter x, defined as

$$S_{x,s} = \frac{1}{s} \cdot \frac{\Delta s}{\Delta x} \ . \tag{21}$$

Depending on the choice of GETI, the required accuracy, and the experimental condition, the experimenter should determine whether the deviation of the estimated temperature ΔT_e is sufficiently small. As an example, we evaluated ΔT_e for B-gTEMP with respect to various condition parameters utilizing this procedure [22].

If one aims to measure temperatures in organelles for comparison using a GETI, it may be necessary to compensate for the difference in conditions among the compartments. One approach to compensation is to measure the calibration standard curves of the GETI under conditions equivalent to those in the organelles. When we performed temperature imaging of the nucleus and cytoplasm in HeLa cells stably expressing ELP-TEMP, we found that the self-concentrations of ELP-TEMP in these compartments were significantly different. Consequently, the dual-band emission ratio of ELP-TEMP responded to temperature differently in the nucleus and cytoplasm [21]. To address this problem, we measured the self-concentrations of ELP-TEMP in the nucleus and cytoplasm using the fluorescence intensity of mVenus (the FRET acceptor) under direct excitation. Subsequently, we measured two calibration standards of ELP-TEMP at these concentrations. Using these calibration standards, we estimated the temperatures in the nucleus and cytoplasm separately and found that the temperatures were minimally different between the two compartments. Additionally, based on our experience, macromolecular crowding [109] may affect the temperature response of GETI, particularly those which involve temperature-induced conformation changes. To adress this issue, in our report on gMELT, we measured the effect of macromolecular crowding on the temperature response of purified gMELT using fluorescence spectroscopy. We then estimated the degree of macromolecular crowding and, consequently, the temperature response curves of gMELT in the cytoplasm, mitochondria, and endoplasmic reticulum through interpolation and maximum likelihood [24].

For dual-band emission ratiometric GETIs involving FRET, the effect of photobleaching on temperature measurement should also be carefully considered [22]. If donor photobleaching occurs, both the donor and acceptor fluorescence intensities decrease. In this case, the error in temperature estimation through the fluorescence ratio may be small. In contrast, if acceptor photobleaching occurs, the donor and acceptor will exhibit, an increase and a decrease in fluorescence intensity, respectively. In this case, the FRET efficiency will appear to decrease, leading to significant error in the fluorescence ratio, and consequently, in temperature estimation. Thus, when using a FRET-based GETI, it is essential to minimize and compensate for photobleaching.

Perspective on thermal biology with GETIs

Bioluminescent GETI

Recently, a growing number of genetically-encoded bioluminescent indicators have been being developed, although no genetically-encoded bioluminescent temperature indicator has been reported in the literature. A bioluminescent indicator contains luciferase, an enzyme that catalyzes the oxidation of its substrate luciferin in the presence of O_2 producing an excited oxidized substrate [110,111]. The excited state of oxidized luciferin transitions to the ground state releasing a luminescence photon. Note that the terms “luciferase” and “luciferin” thereof are generic names that refer to various types of corresponding enzymes and compounds, respectively. Unlike fluorescent indicators, bioluminescent indicators do not require excitation light. In contrast, the excitation light used in fluorescence imaging can cause problems such as phototoxicity to cells, photobleaching of FPs, autofluorescence, and crosstalk of light-induced stimuli. Furthermore, current issues such as low luminescence intensity and limited color variation in bioluminescence are being addressed [110–115]. Importantly, luciferase is compatible with FRET, referred to as bioluminescence resonance energy transfer (BRET) [116]. Therefore, luciferase can be used as a building block for a genetically-encoded indicator based on BRET. As a result, bioluminescent GETIs may emerge in the future.

Heat diffusion coefficients in cells

The heat diffusion coefficient is a measure of how quickly heat dispersion occurs and is one of the key parameters for understanding intracellular thermal processes. It is related to the thermal conductivity κ (W/m·K), heat capacity at constant pressure C_p (J/K·kg), and density ρ (kg/m^3) of a material as:

$$\alpha = \frac{\kappa}{C_p \cdot \rho} \ , \tag{22}$$

where α (m^2/s) is the heat diffusion coefficient. As far as temperature imaging with a GETI is concerned, estimating the thermal conductivity κ at the sub-cellular level may require assumptions or information of the values of C_p, and ρ. However,

these values for all intracellular components are not necessarily available in the literature. Alternatively, the amount of heat supplied to the object of interest may need to be estimated. As a reference, the values of α, κ, C_p, and ρ for pure water at 30 °C are 0.148 mm^2/s, 0.614 W/(m·K), 4.18 kJ/(kg·K), and 996 kg/m^3, respectively. At 40 °C, these values are 0.152 mm^2/s, 0.628 W/(m·K), 4.18 kJ/(kg·K), and 992 kg/m^3, respectively [117].

Several studies have attempted to measure intracellular thermal diffusion coefficients and thermal conductivity. ElAfandy et al. [118] fabricated a gallium nitride nanomembrane-based thermal transport sensor to simultaneously measure the heat diffusion coefficient and the thermal conductivity in cancer cells (MCF-7, MDA-MB-231, SK-BR-3, and HeLa cells). The values were 0.137–0.195 mm^2/s and 0.547–0.577 W/(m·K), respectively. Inomata et al. [119] developed an on-chip-integrated microthermistor and estimated the thermal conductivity in COS-7 cells to be 0.61 W/(m·K). Sotoma et al. [120] employed a heater-thermometer hybrid diamond nanoparticle. The thermal conductivity in HeLa and MCF-7 cells was measured to be 0.11 W/(m·K), which was significantly lower than that of water and corresponded to α = 0.026 mm^2/s, assuming that C_p and ρ were the same as those of water. We also attempted to estimate the intracellular thermal diffusion coefficient using temperature imaging with B-gTEMP [22]. We performed direct imaging of transient heat diffusion in HeLa cells using carbon nanotube clusters as micrometer-sized heat sources. The averaged time trajectory of intracellular temperature was compared with heat diffusion simulation at various values of heat diffusion coefficients to obtain an optimal value of α = 0.027 mm^2/s, which was one-sixth that of water and consistent with the result of Sotoma et al. [120].

A cell can be considered a mixture of water and other materials with varying thermal diffusion coefficients. A textbook on diffusion by Crank introduced Maxwell's equation for addressing diffusion in a continuum medium containing sparsely dispersed spheric components [121], which we apply here to test thermal diffusion. Let α_w and α_x represent the thermal diffusion coefficients of water and component X (e.g., protein, lipid membrane, etc.), respectively. Maxwell's equation is expressed as:

$$\frac{\alpha_{ap}-\alpha_W}{\alpha_{ap}+2\alpha_W}=\phi_X\frac{\alpha_X-\alpha_W}{\alpha_X+2\alpha_W}\ , \tag{23}$$

where the heat diffusion is assumed to occur in a mixture of water and component X, α_{ap} is the apparent thermal diffusion coefficient of the mixture, and ϕ_X is the volume fraction of component X [121]. Note that this equation was derived under steady-state conditions with a sufficiently small value of ϕ_X. By rearranging Equation (23), we obtain:

$$\alpha_{ap}=\frac{\alpha_W\left[(1+2\phi_X)\alpha_X+2(1-\phi_X)\alpha_W\right]}{(1-\phi_X)\alpha_X+(2+\phi_X)\alpha_W}\ , \tag{24}$$

and

$$\frac{d\alpha_{ap}}{d\phi_X}=\frac{3\alpha_W(\alpha_X+2\alpha_W)(\alpha_X-\alpha_W)}{\left[(1-\phi_X)\alpha_X+(2+\phi_X)\alpha_W\right]^2}\ . \tag{25}$$

Therefore, we have $d\alpha_{ap}/d\phi_X < 0$ if $\alpha_x < \alpha_w$ but $d\alpha_{ap}/d\phi_X > 0$ if $\alpha_x > \alpha_w$, because $\alpha_w > 0$ and $\alpha_x > 0$. Considering protein and phospholipid membrane as representative intracellular materials, we crudely estimate that α_{prot} = 0.07 mm^2/s and α_{mem} = 0.09 mm^2/s, where α_{prot} and α_{mem} are the thermal diffusion coefficients for protein and phospholipid membrane, respectively. This indicates that both α_{prot} and α_{mem} are less than α_w (~0.15 mm^2/s). In this calculation, we used values of κ, C_p, and ρ as 0.15 W/(m·K), 1.48 kJ/(kg·K), and 1370 kg/m^3, respectively, for protein, and 0.2 W/(m·K), 2.15 kJ/(kg·K), and 1080 kg/m^3, respectively, for phospholipid membrane [122–126]. Although ϕ_X for protein and phospholipid membrane in a cell may not be sufficiently small, Equation (25) suggests that $\alpha_{ap} < \alpha_w$ under the conditions of $\alpha_{prot} < \alpha_w$ and $\alpha_{mem} < \alpha_w$, if X is composed primarily of protein and phospholipid membrane. In contrast, ElAfandy et al. [118] reported α = 0.161 mm^2/s and 0.195 mm^2/s for MCF-7 and HeLa cells, respectively, both of which are greater than α_w. Furthermore, the results reported by Sotoma et al. [120] and our high-speed temperature imaging [22] showed α = 0.026–0.027 mm^2/s, which is considerably smaller than α_w and may not be plausibly explained by Equation (24) using conventional thermal parameter values for intracellular components. Thus, the data on intracellular thermal diffusion coefficients suggest that intracellular thermal dynamics are far more intricate and significantly different from a simple mixture model like Equation (23). Additionally, with respect to intracellular thermal diffusion, Suzuki and Plakhotnik considered thermal boundary resistance, also known as Kapitza resistance, and proposed an explanation for the low intracellular thermal conductivity value of κ = 0.1 W/(m·K) [127]. To better understand intracellular thermal processes,

we believe that further investigations will be necessary in the future, incorporating more accurate intracellular temperature measurements and more realistic modeling of intracellular thermal transport.

The 10^5-gap issue

Many studies of intracellular temperatures using fluorescent nanothermometers have reported increases in temperature of more than 1 K inside cultured cells following chemical stimulation with drugs such as FCCP and CCCP. These findings were summarized in review papers by Macherel et al. [6], Zhou et al. [39], and Suzuki and Plakhotnik [127]. In contrast, Baffou et al. challenged these observations of intracellular temperature increases from the standpoint of heat transport physics [128]. They presented an approximate steady-state solution to the heat diffusion equation for a heat-generating object immersed in a medium, expressed as:

$$\Delta T = \frac{P}{\kappa \cdot L} \ , \tag{26}$$

where ΔT, P, κ, and L represent the temperature increase, heat generation power, thermal conductivity, and size or diameter of the object, respectively. The thermal conductivity of the medium was assumed to be the same as that of the object. Using test values of P~100 pW/cell, κ ~1 W/(m·K), and L~10 μm, ΔT was calculated to be approximately 10^{-5} K. Therein, Baffou et al. stated, "Such substantial temperature variations cannot physically result from thermogenesis, which casts doubt on the interpretation of the results" [128]. The inconsistency between the order of magnitude of ΔT measured in experiments and that calculated using heat transport physics in Equation (26) was denoted as the 10^5-gap issue by Suzuki et al. [129].

Because the fluorescence response of fluorescent nanothermometers including GETIs could be susceptible to crosstalk between temperature and other environmental changes, studies using fluorescent nanothermometers might not ultimately rule out the possibility of such crosstalk in experimental results. However, many studies have recognized this issue, and experimental researchers have made significant efforts to test controls, estimate uncertainties, and mitigate the problem. Furthermore, it is noteworthy that such noticeable temperature increases in cells have been observed not only in studies using fluorescent nanothermometers but also with other temperature measurement techniques, such as thermocouples, bimetal probes, and Raman spectroscopy [130–132].

We also agree that Baffou's formula (Equation (26)) is valid as long as its prerequisite can be applied to the situation of interest. However, considering many experimental results mentioned above, we believe that the interpretation of intracellular temperature increases reported in these studies cannot necessarily be ruled out. Instead, the prerequisite for Baffou's formula (Equation (26)) may be questioned in certain cases. Additionally, Suzuki et al. argued that if more precise values of variables, such as heat sources in stimulated cells, length scales, and thermal parameters on the nanometer to micrometer scale, are considered, then the 10^5-gap issue may be resolved at least partly [129]. Considering these situations, we speculate that certain factors may still be unknown or not precisely understood, preventing a complete explanation of intracellular temperature changes upon stimulation. Furthermore, we believe that further studies on subjects such as intracellular thermal parameters, thermal phenomena at the nanometer to micrometer scale, and intracellular heat sources will be necessary. These studies may help resolve the controversy surrounding the 10^5-gap issue in the future.

Local temperature and heat perturbation

An important advantage of temperature imaging using fluorescence microscopy is its ability to visualize intracellular temperature distribution at optical microscopy resolution. In this context, temperature imaging studies have often focused on local temperature variations or hot spots in living cells. Several studies have attempted to observe local temperatures in intracellular compartments, such as cytoplasm, nucleus, and mitochondria, under steady-state condition or during physiological responses without the addition of artificial agents like CCCP or FCCP, although the results remain inconclusive. Previous studies using fluorescent polymeric thermometers (FPTs) for fluorescence lifetime imaging microscopy (FLIM) reported that the temperature in nucleus was approximately 1 K higher than that in cytoplasm of COS7 and HeLa cells [35,37]. Piñol et al. conducted temperature imaging using nanothermometers based on luminescent lanthanoid complex-bearing polymeric micelles and reported that the temperature in the nucleolus of breast cancer MDA-MB-468 cells was 5 K higher than in the rest of the cell [133]. Chuma et al. investigated temperatures in neuron-like PC12 cells using FPTs and fluorescent nanodiamonds via FLIM and optically detected magnetic resonance microscopy. They observed that the temperature in the nucleus of pre-differentiated PC12 cells was higher than that in the cytoplasm and that temperatures in both the nucleus and cytoplasm increased following the addition of nerve growth factor [134]. In addition, previously, we also attempted to observe HeLa cells by using gTEMP to suggest a 2.9 K higher temperature in nucleus than in cytoplasm [17], but in our more recent re-examinations using ELP-TEMP and B-gTEMP we could not detect noticeable temperature difference between the two sub-cellular compartments [21,22].

Mitochondrial thermogenesis has also been extensively investigated, as mitochondria are organelles involved in key

metabolic pathways and futile cycles that generate substantial heat, and are therefore thought to potentially exhibit noticeably high temperatures. In terms of local temperature, studies by Chrétien et al. [135,136] have attracted significant attention. They used MitoThermo Yellow, a temperature-responsive organic dye that specifically targets mitochondria, and detected a fluorescence signal corresponding to a temperature increase of 10 K above the medium temperature during full activation of respiratory chain in human embryonic kidney 293 cells, primary skin fibroblasts, and HeLa cells [135,136]. Additionally, Terzioglu et al. used MitoThermo Yellow and gTEMP to confirm these observation of hot mitochondria in mammalian and insect cells through fluorescence spectroscopy and fluorescence microscopy, and observed temperature decreases following the application of various respiratory chain inhibitors [137]. Although the temperature measurements by Chrétien et al. and Terzioglu et al. appear to have been carefully conducted to infer such mitochondrial temperatures, the authors themselves cautiously noted, "these observations need to be further validated and explored by independent methods" [135] and "it is obviously desirable that all conclusions arising from our and similar studies should be independently verified using different approaches" [137]. Among the papers citing the work by Chrétien et al. [135], two gave it serious consideration. Fahimi and Matta theoretically examined the thermal conductance of ATP synthase in the inner mitochondrial membrane, drawing an analogy to a ratchet engine and considering the processes of protonation, hydration, and thermalization of protons permeating through ATP synthase, in an attempt to rationalize the elevated mitochondrial temperature [138]. In contrast, Macherel et al. considered heat transfer physics, including Fourier's law and nanoscale heat effects, and concluded "The analysis shows that the temperature elevation within the mitochondrial volume indicated no singularity and that it is nonphysical to detect an increase of temperature of about ~1 K, as observed in mitochondria for the estimated power dissipated by the numerous chemical reactions occurring in mitochondria" [6]. In our opinion, we agree with Chrétien et al. [135,136] and Terzioglu et al. [137] that intracellular hot spots, such as hot mitochondria, should be further validated independently using various approaches. However, if the observation of hot mitochondria is further supported by future intensive investigations, the physical and biological models, along with the parameter values assumed by Baffou et al. [128] and Macherel et al. [6], should be critically re-examined. In science, it is well known that exceptions sometimes lead to discoveries, whether large or small. Alongside the 10^5-gap issue, hot mitochondria could represent one such exception.

Intracellular local temperature may be associated with a variety of cellular processes. Chung et al. investigated the effect of the 42-residue variant of amyloid-β (Aβ42), which is implicated in neurodegenerative diseases, in HEK293T cells and found that the intracellular temperature increased by 2.8 K upon the addition of Aβ42, likely due to its exothermic aggregation rather than mitochondrial damage [139]. They suggested that Aβ42 aggregation in a cell may create a hotspot, which in turn could overcome the energy barrier for subsequent Aβ42 nucleation, leading to further aggregation. Additionally, although temperature imaging studies have primarily focused on relatively large temperature differences, (e.g. >0.1 K), it is important to note that temperature differences or gradients at subcellular scales can often be much smaller. A previous optical radiometry study of the pit organ in pit vipers suggested that the sensory endings on the pit membrane can respond to temperature contrasts as small as ≤1 mK [140], and that the thermo-responsive TRPA1 channel in the nerve fibers plays a key role in the signal transduction [141]. Graf and Machta proposed a mechanism by which information from many TRPA1 molecules is integrated through bifurcation dynamics, reproducing the mK-level temperature sensitivity observed in TRPA1-dependent action potential frequency [142]. This suggests that numerous intracellular processes may subtly respond to small temperature differences and fluctuations, and that such thermal events may play important roles in mediating processes such as signal transduction.

In addition to observing local temperatures in cells, numerous studies have explored heat perturbation at the subcellular scale to investigate the effects of local temperature increases on cellular functions. Ferdinandus et al. developed a polymeric nanoparticle called nanoHT, in which fluorescent temperature-sensitive dyes and photothermal dyes were embedded in a poly(methylmethacrylate-*co*-methacrylic acid) polymer matrix, to examine cell death, intracellular ATP dynamics, and C2C12 myotube contraction induced by local heating [143]. More recently, Chuma et al. employed a near-infrared 1475 nm laser for local heating at the subcellular scale to investigate the differentiation of neuron-like PC12 cells and primary mouse cortical neurons [134]. Because these heat perturbation techniques utilize photothermal conversion to locally generate heat, they are useful for applying heat precisely at specific positions and times, in contrast to simply adding drugs to a culture medium in a Petri dish on a microscope stage. Thus, this new approach of combining local heat perturbation with temperature imaging is likely to pave the way for new discoveries in cell biology.

Joule heating

In animals, heat production is traditionally thought to occur through shivering and non-shivering thermogenesis [1], with the heat generated by these mechanisms generally considered a direct result of reaction heat. Beyond this conventional view of thermogenesis, we recently proposed a novel mechanism of thermogenesis: Joule heating associated with ion transport [26]. Ion currents through channel proteins and ion transporter proteins are ubiquitous in cellular and organelle membranes. Due to the membrane potential across the membranes, transported ions experience a voltage difference, which results in the generation of Joule heat (Figure 9). Before our proposal [26], this concept was largely

overlooked in biology. We theoretically investigated Joule heating associated with ion transport and predicted that biological ion transport across membranes can result in not only heat production but also heat absorption, depending on the direction of the ion current (Figure 9). Based on this concept, we demonstrated that Joule heating likely provides insights into heat production and absorption in nerve cells during action potentials and non-shivering thermogenesis involving BATM.

Although our paper on Joule heating [26] covered the thermogenesis of a single channel, nerve cells, and BATM, many other heat-related phenomena involving Joule heating likely exist, as ion transport is highly ubiquitous in biology. As we proposed the significance of Joule heating in biology solely on a theoretical basis in our paper [26], Joule heating should also be scrutinized experimentally to advance our understanding. Considering that Joule heating is relevant to ion transport protein, measuring local temperature change around these proteins would be helpful. To meet this requirement, GETIs among fluorescent nanothermometers would be particularly useful, as a GETI can be fused with a specific signal polypeptide or protein to achieve precise localization within cells. Additionally, considering that ion currents through channel proteins are often turned on and off on the timescale of milliseconds or less [144], a nanothermometer capable of responding to temperature changes on the same timescale is required. Although B-gTEMP [22] may be a potential GETI for such experiments, its temperature sensitivity should ideally be significantly improved. Accordingly, while current GETIs are useful temperature indicators for investigating Joule heating, we anticipate significant improvements in the performance of GETIs, as well as in measurement methods for advancing thermal biology studies in the future.

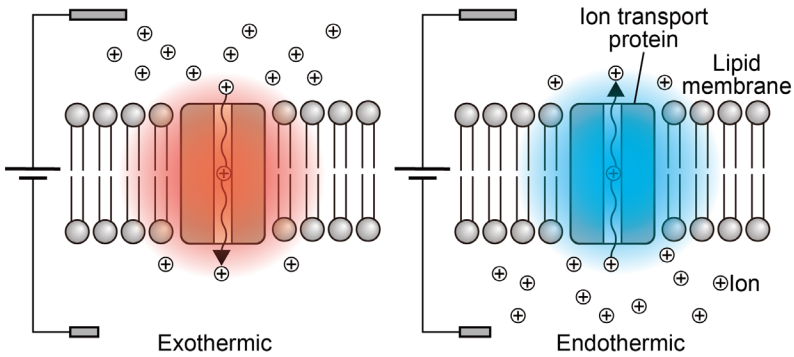

Figure 9 Joule heating involving an ion transport protein. (Left) If an ion current occurs in the forward direction with respect to the potential difference, then heat production is expected. (Right) If an ion current occurs in the backward direction, then heat absorption is expected. Adapted from Wazawa and Nagai [26].

Conflict of Interest

The authors declare no conflict of interest.

Author Contributions

Tetsuichi Wazawa: Conceptualization (equal), writing–original draft (lead), writing–review & editing (equal), visualization. Ryohei Ozaki-Noma: Writing–original draft (supporting). Lu Kai: Writing–original draft (supporting). Shun-ichi Fukushima: Writing–original draft (supporting). Tomoki Matsuda: Conceptualization (supporting). Takeharu Nagai: Conceptualization (equal), writing–review & editing (equal), supervision.

Data Availability

The data presented in this paper are available from the corresponding author upon reasonable request.

Acknowledgements

We are grateful to Dr. Kazunori Sugiura at SANKEN, Osaka University, for helpful comments on fluorescent proteins and protein engineering. This work was in part supported by grants from Core Research for Evolutionary Science and Technology, Japan Science and Technology Agency (JPMJCR15N3 to TN), Japan Society for the Promotion of Science (23115003, 18H03987, 18H05410, 21K19225, and 23H05421 to TN; 19K05226 and 22K04891 to TW; 23KJ1492 to RON), The Naito Foundation (to TN), The Sumitomo Foundation (to TN), and the Research Program of “Dynamic Alliance for Open Innovation Bridging Human, Environment (to TN).

References

[1] Himms-Hagen, J. Cellular thermogenesis. Annu. Rev. Physiol. 38, 315–351 (1976). https://doi.org/10.1146/annurev.ph.38.030176.001531

[2] Cannon, B., Nedergaard, J. Brown adipose tissue: Function and physiological significance. Physiol. Rev. 84, 277–359 (2004). https://doi.org/10.1152/physrev.00015.2003

[3] Nakano, M., Nagai, T. Thermometers for monitoring cellular temperature. J. Photochem. Photobiol. C-Photochem. Rev. 30, 2–9 (2017). https://doi.org/10.1016/j.jphotochemrev.2016.12.001

[4] Okabe, K., Sakaguchi, R., Shi, B., Kiyonaka, S. Intracellular thermometry with fluorescent sensors for thermal biology. Pflügers Arch. Eur. J. Physiol. 470, 717–731 (2018). https://doi.org/10.1007/s00424-018-2113-4

[5] Wang, M., Da, Y., Tian, Y. Fluorescent proteins and genetically encoded biosensors. Chem. Soc. Rev. 52, 1189–1214 (2023). https://doi.org/10.1039/D2CS00419D

[6] Macherel, D., Haraux, F., Guillou, H., Bourgeois, O. The conundrum of hot mitochondria. Biochim. Biophys. Acta Bioenerg. 1862, 148348 (2021). https://doi.org/10.1016/j.bbabio.2020.148348

[7] Kemp, R. B. Calorimetric studies of heat flux in animal cells. Thermochim. Acta, 193, 253–267 (1991). https://doi.org/10.1016/0040-6031(91)80187-N

[8] Alberty, R. A., Cornish-Bowden, A., Goldberg, R. N., Hammes, G. G., Tipton, K., Westerhoff, H. V. Recommendations for terminology and databases for biochemical thermodynamics. Biophys. Chem. 155, 89–103 (2011). https://doi.org/10.1016/j.bpc.2011.03.007

[9] Alberty, R. A. Calculation of standard transformed Gibbs energies and standard transformed enthalpies of biochemical reactants. Arch. Biochem. Biophys. 353, 116–130 (1998). https://doi.org/10.1006/abbi.1998.0638

[10] Naik, R. R., Kirkpatrick, S. M., Stone, M. O. The thermostability of an alpha-helical coiled-coil protein and its potential use in sensor applications. Biosens. Bioelectron. 16, 1051–1057 (2001). https://doi.org/10.1016/s0956-5663(01)00226-3

[11] Wong, F. H., Banks, D. S., Abu-Arish, A., Fradin, C. A molecular thermometer based on fluorescent protein blinking. J. Am. Chem. Soc. 129, 10302–10303 (2007). https://doi.org/10.1021/ja0715905

[12] Kamei, Y., Suzuki, M., Watanabe, K., Fujimori, K., Kawasaki, T., Deguchi, T., et al. Infrared laser–mediated gene induction in targeted single cells in vivo. Nat. Methods 6, 79–81 (2009). https://doi.org/10.1038/nmeth.1278

[13] Donner, J. S., Thompson, S. A., Kreuzer, M. P., Baffou, G., Quidant, R. Mapping intracellular temperature using green fluorescent protein. Nano Lett. 12, 2107–2111 (2012). https://doi.org/10.1021/nl300389y

[14] Donner, J. S., Thompson, S. A., Alonso-Ortega, C., Morales, J., Rico, L. G., Santos, S. I., et al. Imaging of plasmonic heating in a living organism. ACS Nano 7, 8666–8672 (2013). https://doi.org/10.1021/nn403659n

[15] Kiyonaka, S., Kajimoto, T., Sakaguchi, R., Shinmi, D., Omatsu-Kanbe, M., Matsuura, H., et al. Genetically encoded fluorescent thermosensors visualize subcellular thermoregulation in living cells. Nat. Methods 10, 1232–1238 (2013). https://doi.org/10.1038/nmeth.2690

[16] Deepankumar, K., Nadarajan, S. P., Bae, D. H., Baek, K. H., Choi, K. Y., Yun, H. Temperature sensing using red fluorescent protein. Biotechnol. Bioprocess Eng. 20, 67–72 (2015). https://doi.org/10.1007/s12257-014-0456-z

[17] Nakano, M., Arai, Y., Kotera, I., Okabe, K., Kamei, Y., Nagai, T. Genetically encoded ratiometric fluorescent thermometer with wide range and rapid response. PLoS One 12, e0172344 (2017). https://doi.org/10.1371/journal.pone.0172344

[18] Savchuk, O. A., Silvestre, O. F., Adão, R. M. R., Nieder, J. B. GFP fluorescence peak fraction analysis based nanothermometer for the assessment of exothermal mitochondria activity in live cells. Sci. Rep. 9, 7535 (2019). https://doi.org/10.1038/s41598-019-44023-7

[19] Maksimov, E. G., Yaroshevich, I. A., Tsoraev, G. V., Sluchanko, N. N., Slutskaya, E. A., Shamborant, O. G., et al. A genetically encoded fluorescent temperature sensor derived from the photoactive Orange Carotenoid Protein. Sci Rep. 9, 8937 (2019). https://doi.org/10.1038/s41598-019-45421-7

[20] Silva, P. L., Savchuk, O. A., Gallo, J., García-Hevia, L., Bañobre-López, M., Nieder, J. B. Mapping intracellular thermal response of cancer cells to magnetic hyperthermia treatment. Nanoscale 12, 21647–21656 (2020). https://doi.org/10.1039/c9nr10370h

[21] Vu, C. Q., Fukushima, S., Wazawa, T., Nagai, T. A highly-sensitive genetically encoded temperature indicator exploiting a temperature-responsive elastin-like polypeptide. Sci Rep. 11, 16519 (2021). https://doi.org/10.1038/s41598-021-96049-5

[22] Lu, K., Wazawa, T., Sakamoto, J., Vu, C. Q., Nakano, M., Kamei, Y., et al. Intracellular heat transfer and thermal property revealed by kilohertz temperature imaging with a genetically encoded nanothermometer. Nano Lett. 22, 5698–5707 (2022). https://doi.org/10.1021/acs.nanolett.2c00608

[23] Sorenson, A. E., Schaeffer, P. M. Real-time temperature sensing using a ratiometric dual fluorescent protein biosensor. Biosensors 13, 338 (2023). https://doi.org/10.3390/bios13030338

[24] Fukushima, S., Wazawa, T., Sugiura, K., Nagai, T. Extremely sensitive genetically encoded temperature indicator enabling measurement at the organelle level. ACS Sens. 9, 3889–3897 (2024). https://doi.org/10.1021/acssensors.3c02658
[25] Klotz, I. M., Robert, M., Rosenberg, R. M. Chemical thermodynamics: Basic concepts and methods. 5th Ed. (Wiley, New York, 1994).
[26] Wazawa, T., Nagai, T. Joule heating involving ion currents through channel proteins. Biophys. Physicobiol. 20, e200030 (2023). https://doi.org/10.2142/biophysico.bppb-v20.0030
[27] Hemingway, A. Shivering. Physiol. Rev. 43, 397–422 (1963). https://doi.org/10.1152/physrev.1963.43.3.397
[28] Rowland, L. A., Bal, N. C., Periasamy, M. The role of skeletal-muscle-based thermogenic mechanisms in vertebrate endothermy. Biol. Rev. Camb. Philos. Soc. 90, 1279–1297 (2015). https://doi.org/10.1111/brv.12157
[29] Tseng, Y.-H., Cypess, A. M., Kahn, C. R. Nat. Rev. Drug Discov. 9, 465–482 (2010). https://doi.org/10.1038/nrd3138
[30] Roesler, A., Kazak, L. UCP1-independent thermogenesis. Biochem. J. 477, 709–725 (2020). https://doi.org/10.1042/BCJ20190463
[31] Bertholet, A. M., Kirichok, Y. Mitochondrial H^+ leak and thermogenesis. Annu. Rev. Physiol. 84, 381–407 (2022). https://doi.org/10.1146/annurev-physiol-021119-034405
[32] Nicholls, D. G. Mitochondrial proton leaks and uncoupling proteins. Biochim. Biophys. Acta Bioenerg. 1862, 148428 (2021). https://doi.org/10.1016/j.bbabio.2021.148428
[33] Barreto, P., Couñago, R. M., Arruda, P. Mitochondrial uncoupling protein-dependent signaling in plant bioenergetics and stress response. Mitochondrion 53, 109–120 (2020). https://doi.org/10.1016/j.mito.2020.05.001
[34] Moore, A. L., Shiba, T., Young, L., Harada, S., Kita, K., Ito, K. Unraveling the heater: New insights into the structure of the alternative oxidase. Annu. Rev. Plant Biol. 64, 637–663 (2013). https://doi.org/10.1146/annurev-arplant-042811-105432
[35] Okabe, K., Inada, N., Gota, C., Harada, Y., Funatsu, T., Uchiyama, S. Intracellular temperature mapping with a fluorescent polymeric thermometer and fluorescence lifetime imaging microscopy. Nat. Commun. 3, 705 (2012). https://doi.org/10.1038/ncomms1714
[36] Kriszt, R., Arai, S., Itoh, H., Lee, M. H., Goralczyk, A. G., Ang, X. M., et al. Optical visualisation of thermogenesis in stimulated single-cell brown adipocytes. Sci. Rep. 7, 1383 (2017). https://doi.org/10.1038/s41598-017-00291-9
[37] Hayashi, T., Fukuda, N., Uchiyama, S., Inada, N. A cell-permeable fluorescent polymeric thermometer for intracellular temperature mapping in mammalian cell lines. PLoS One 10, e0117677 (2015). https://doi.org/10.1371/journal.pone.0117677
[38] Tanimoto, R., Hiraiwa, T., Nakai, Y., Shindo, Y., Oka, K., Hiroi, N., et al. Detection of temperature difference in neuronal cells. Sci. Rep. 6, 22071 (2016). https://doi.org/10.1038/srep22071
[39] Zhou, J., Del Rosal, B., Jaque, D., Uchiyama, S., Jin, D. Advances and challenges for fluorescence nanothermometry. Nat. Methods 17, 967–980 (2020). https://10.1038/s41592-020-0957-y
[40] Nicholls, D. G., Ferguson, S. J. Bioenergetics 4th Ed. (Academic Press, London, 2013).
[41] Lakowicz, J. R. Principles of fluorescence spectroscopy, 3rd Ed. (Springer, New York, 2006).
[42] Nienhaus, K., Nienhaus, G. U. Chromophore photophysics and dynamics in fluorescent proteins of the GFP family. J. Phys. Condens. Matter. 28, 443001 (2016). https://doi.org/10.1088/0953-8984/28/44/443001
[43] Balzani, V., Ceroni, P., Juris, A. Photochemistry and photophysics: Concepts, research, applications. (Wiley-VCH, Weinheim, 2014).
[44] Niwa, H., Inouye, S., Hirano, T., Matsuno, T., Kojima, S., Kubota, M., et al. Chemical nature of the light emitter of the Aequorea green fluorescent protein. Proc. Natl. Acad. Sci. U.S.A. 93, 13617–13622 (1996). https://doi.org/10.1073/pnas.93.24.13617
[45] Patterson, G. H., Knobel, S. M., Sharif, W. D., Kain, S. R., Piston, D. W. Use of the green fluorescent protein and its mutants in quantitative fluorescence microscopy. Biophys. J. 73, 2782–2790 (1997). https://doi.org/10.1016/S0006-3495(97)78307-3
[46] Cormack, B. P., Valdivia, R. H., Falkow, S. FACS-optimized mutants of the green fluorescent protein (GFP). Gene 173, 33–38 (1996). https://doi.org/10.1016/0378-1119(95)00685-0
[47] Shaner, N. C., Lambert, G. G., Chammas, A., Ni, Y., Cranfill, P. J., Baird, M. A., et al. A bright monomeric green fluorescent protein derived from *Branchiostoma lanceolatum*. Nat. Methods 10, 407–409 (2013). https://doi.org/10.1038/nmeth.2413
[48] Wardle, B. Principles and applications of photochemistry. (Wiley, West Sussex, 2009).
[49] Byrdin, M., Duan, C., Bourgeois, D., Brettel, K. A long-lived triplet state is the entrance gateway to oxidative photochemistry in green fluorescent proteins. J. Am. Chem. Soc. 140, 2897–2905 (2018). http://doi.org/10.1021/jacs.7b12755

[50] Taylor, M. A., Zhu, L., Rozanov, N. D., Stout, K. T., Chen, C., Fang, C. Delayed vibrational modulation of the solvated GFP chromophore into a conical intersection. Phys. Chem. Chem. Phys. 21, 9728–9739 (2019). https://doi.org/10.1039/c9cp01077g
[51] Olsen, S., Smith, S. C. Radiationless decay of red fluorescent protein chromophore models via twisted intramolecular charge-transfer states. J. Am. Chem. Soc. 129, 2054–2065 (2007). https://doi.org/10.1021/ja066430s
[52] dos Santos, A. M. Thermal effect on Aequorea green fluorescent protein anionic and neutral chromophore forms fluorescence. J. Fluoresc. 22, 151–154 (2012). https://doi.org/10.1007/s10895-011-0941-0
[53] Lombardi, J. R., Raymonda, J. W., Albrecht, A. C. Rotational relaxation in rigid media by polarized photoselection. J. Chem. Phys. 40, 1148–1156 (1964) https://doi.org/10.1063/1.1725264
[54] Valiev, K. A., Ivanov E. N. Rotational brownian motion. Sov. Phys. Usp. 16, 1–16 (1973). https://doi.org/10.1070/PU1973v016n01ABEH005145
[55] Debye, P. Polar molecules. (Chemical Catalog, New York, 1929).
[56] Kinosita, K. Jr., Kawato, S., Ikegami, A. A theory of fluorescence polarization decay in membranes. Biophys. J. 20, 289–305 (1977). https://doi.org/10.1016/s0006-3495(77)85550-1
[57] Lipari, G., Szabo, A. Effect of librational motion on fluorescence depolarization and nuclear magnetic resonance relaxation in macromolecules and membranes. Biophys. J. 30, 489–506 (1980). https://doi.org/10.1016/S0006-3495(80)85109-5
[58] Wazawa, T., Morimoto, N., Nagai, T., Suzuki, M. Rotational motion of rhodamine 6G tethered to actin through oligo(ethylene glycol) linkers studied by frequency-domain fluorescence anisotropy. Biophys. Physicobiol. 12, 87–102 (2015). https://doi.org/10.2142/biophysico.12.0_87
[59] Teijeiro-Gonzalez, Y., Crnjar, A., Beavil, A. J., Beavil, R. L., Nedbal, J., Le Marois A. et al. Time-resolved fluorescence anisotropy and molecular dynamics analysis of a novel GFP homo-FRET dimer. Biophys J. 120, 254–269 (2021). https://doi.org/10.1016/j.bpj.2020.11.2275
[60] Koski, P., Saarilahti, H., Sukupolvi, S., Taira, S., Riikonen, P., Osterlund, K., et al. A new alpha-helical coiled coil protein encoded by the Salmonella typhimurium virulence plasmid. J. Biol. Chem. 267, 12258–12265 (1992). https://doi.org/10.1016/S0021-9258(19)49833-5
[61] Varanko, A. K., Su, J. C., Chilkoti, A. Elastin-like polypeptides for biomedical applications. Annu. Rev. Biomed. Eng. 22, 343–369 (2020). https://doi.org/10.1146/annurev-bioeng-092419-061127
[62] Muzzopappa, F., Kirilovsky, D. Changing color for photoprotection: The Orange Carotenoid Protein. Trends Plant Sci. 25, 92–104 (2020). https://doi.org/10.1016/j.tplants.2019.09.013
[63] Hurme, R., Berndt, K. D., Normark, S. J., Rhen, M. A proteinaceous gene regulatory thermometer in Salmonella. Cell 90, 55–64 (1997). https://doi.org/10.1016/s0092-8674(00)80313-x
[64] Piraner, D. I., Abedi, M. H., Moser, B. A., Lee-Gosselin, A., Shapiro, M. G. Tunable thermal bioswitches for in vivo control of microbial therapeutics. Nat. Chem. Biol. 13, 75–80 (2017). https://doi.org/10.1038/nchembio.2233
[65] Piraner, D. I., Wu, Y., Shapiro, M. G. Modular thermal control of protein dimerization. ACS Synth. Biol. 8, 2256–2262 (2019). https://doi.org/10.1021/acssynbio.9b00275
[66] Demchenko, A. P. The concept of λ-ratiometry in fluorescence sensing and imaging. J. Fluoresc. 20, 1099–1128 (2010). https://doi.org/10.1007/s10895-010-0644-y
[67] Kinosita, K. Jr., Itoh, H., Ishiwata, S., Hirano, K., Nishizaka, T., Hayakawa, T. Dual-view microscopy with a single camera: Real-time imaging of molecular orientations and calcium. J. Cell Biol. 115, 67–73 (1991). https://doi.org/10.1083/jcb.115.1.67
[68] Axelrod, D. Fluorescence polarization microscopy. Methods Cell Biol. 30, 333–352 (1989). https://doi.org/10.1016/S0091-679X(08)60985-1
[69] Kim, S. Y., Arai, Y., Tani, T., Takatsuka, H., Saito, Y., Kawashima, T., et al. Simultaneous imaging of multiple cellular events using high-accuracy fluorescence polarization microscopy. Microscopy 66, 110–119 (2017). https://doi.org/10.1093/jmicro/dfw110
[70] Inoué, S., Spring, K. R. Video microscopy: The fundamentals, 2nd Ed. (Plenum, New York, 1997).
[71] van Zanten, T. S., Pradeep, S. G., Mayor, S. Quantitative fluorescence emission anisotropy microscopy for implementing homo-fluorescence resonance energy transfer measurements in living cells. Mol. Biol. Cell 34, 6 (2023). https://doi.org/10.1091/mbc.E22-09-0446
[72] Shinoda, H., Ma, Y., Nakashima, R., Sakurai, K., Matsuda, T., Nagai, T. Acid-tolerant monomeric GFP from *Olindias formosa*. Cell Chem. Biol. 25, 330–338 (2018). https://doi.org/10.1016/j.chembiol.2017.12.005
[73] Daune, M. Molecular biophysics: Structures in motion. (Oxford University Press, Oxford, 1999).
[74] Shcherbakova, D. M., Sengupta, P., Lippincott-Schwartz, J., Verkhusha, V. V. Photocontrollable fluorescent proteins for superresolution imaging. Annu. Rev. Biophys. 43, 303–329 (2014). https://doi.org/10.1146/annurev-biophys-051013-022836

[75] Pace, C. N., Grimsley, G. R., Scholtz, J. M. Protein ionizable groups: pK values and their contribution to protein stability and solubility. J. Biol. Chem. 284, 13285–13289 (2009). https://doi.org/10.1074/jbc.R800080200
[76] Duan, C., Adam, V., Byrdin, M., Ridard, J., Kieffer-Jaquinod, S., Morlot, C., et al. Structural evidence for a two-regime photobleaching mechanism in a reversibly switchable fluorescent protein. J. Am. Chem. Soc. 135, 15841–15850 (2013). https://doi.org/10.1021/ja406860e
[77] Mamontova, A. V., Grigoryev, A. P., Tsarkova, A. S., Lukyanov, K. A., Bogdanov, A. M. Struggle for photostability: Bleaching mechanisms of fluorescent proteins. Russ. J. Bioorg. Chem. 43, 625–633 (2017). https://doi.org/10.1134/S1068162017060085
[78] Hirano, M., Ando, R., Shimozono, S., Sugiyama, M., Takeda, N., Kurokawa, H., et al. A highly photostable and bright green fluorescent protein. Nat. Biotechnol. 40, 1132–1142 (2022). https://doi.org/10.1038/s41587-022-01278-2
[79] Fosque, B. F., Sun, Y., Dana, H., Yang, C. T., Ohyama, T., Tadross, M. R., et al. Neural circuits: Labeling of active neural circuits in vivo with designed calcium integrators. Science 347, 755–760 (2015). https://doi.org/10.1126/science.1260922
[80] Bourgeois, D., Adam, V. Reversible photoswitching in fluorescent proteins: A mechanistic view. IUBMB Life 64, 482–491 (2012). https://doi.org/10.1002/iub.1023
[81] Bierbuesse, F., Bourges, A. C., Gielen, V., Mönkemöller, V., Vandenberg, W., Shen, Y., et al. Absolute measurement of cellular activities using photochromic single-fluorophore biosensors and intermittent quantification. Nat. Commun. 13, 1850 (2022). https://doi.org/10.1038/s41467-022-29508-w
[82] Wazawa, T., Noma, R., Uto, S., Sugiura, K., Washio, T., Nagai, T. A photoswitchable fluorescent protein for hours-time-lapse and sub-second-resolved super-resolution imaging. Microscopy 70, 340–352 (2021). https://doi.org/10.1093/jmicro/dfab001
[83] Kao, Y. T., Zhu, X., Min, W. Protein-flexibility mediated coupling between photoswitching kinetics and surrounding viscosity of a photochromic fluorescent protein. Proc. Natl. Acad. Sci. U.S.A. 109, 3220–3225 (2012). https://doi.org/10.1073/pnas.1115311109
[84] Gräwe, A., Stein, V. Linker engineering in the context of synthetic protein switches and sensors. Trends Biotechnol. 39, 731–744 (2021). https://doi.org/10.1016/j.tibtech.2020.11.007
[85] Chen, X., Zaro, J. L., Shen, W. C. Fusion protein linkers: Property, design and functionality. Adv. Drug. Deliv. Rev. 65, 1357–1369 (2013). https://doi.org/10.1016/j.addr.2012.09.039
[86] Vidal, L. S., Isalan, M., Heap, J. T., Ledesma-Amaro, R. A primer to directed evolution: current methodologies and future directions. RSC Chem. Biol. 4, 271–291 (2023). https://doi.org/10.1039/d2cb00231k
[87] Tiwari, D. K., Arai, Y., Yamanaka, M., Matsuda, T., Agetsuma, M., Nakano, M., et al. A fast- and positively photoswitchable fluorescent protein for ultralow-laser-power RESOLFT nanoscopy. Nat. Methods 12, 515–518 (2015). https://doi.org/10.1038/nmeth.3362
[88] McCullum, E. O., Williams, B. A., Zhang, J., Chaput, J. C. Random mutagenesis by error-prone PCR. Methods Mol. Biol. 634, 103–109 (2010). https://doi.org/10.1007/978-1-60761-652-8_7
[89] Emond, S., Petek, M., Kay, E. J., Heames, B., Devenish, S. R. A., Tokuriki, N., et al. Accessing unexplored regions of sequence space in directed enzyme evolution via insertion/deletion mutagenesis. Nat. Commun. 11, 3469 (2020). https://doi.org/10.1038/s41467-020-17061-3
[90] Cadwell, R. C., Joyce, G. F. Randomization of genes by PCR mutagenesis. Genome Res. 2, 28–33 (1992). https://doi.org/10.1101/gr.2.1.28
[91] Higuchi, R., Krummel, B., Saiki, R. K. A general method of in vitro preparation and specific mutagenesis of DNA fragments: Study of protein and DNA interactions. Nucleic Acids Res. 16, 7351–7367 (1988). https://doi.org/10.1093/nar/16.15.7351
[92] Zhao, H., Giver, L., Shao, Z., Affholter, J. A., Arnold, F. H. Molecular evolution by staggered extension process (StEP) in vitro recombination. Nat. Biotechnol. 16, 258–261 (1998). https://doi.org/10.1038/nbt0398-258
[93] Heinemann, U., Hahn, M. Circular permutation of polypeptide chains: Implications for protein folding and stability. Prog. Biophys. Mol. Biol. 64, 121–143 (1995). https://doi.org/10.1016/0079-6107(95)00013-5
[94] Nagai, T., Yamada, S., Tominaga, T., Ichikawa, M., Miyawaki, A. Expanded dynamic range of fluorescent indicators for Ca^{2+} by circularly permuted yellow fluorescent proteins. Proc. Natl. Acad. Sci. U.S.A. 101, 10554–10559 (2004). https://doi.org/10.1073/pnas.0400417101
[95] Kostyuk, A. I., Demidovich, A. D., Kotova, D. A., Belousov, V. V., Bilan, D. S. Circularly permuted fluorescent protein-based indicators: History, principles, and classification. Int. J. Mol. Sci. 20, 4200 (2019). https://doi.org/10.3390/ijms20174200
[96] Wiseman, D. N., Otchere, A., Patel, J. H., Uddin, R., Pollock, N. L., Routledge, S. J., et al. Expression and purification of recombinant G protein-coupled receptors: A review. Protein Expr. Purif. 167, 105524 (2020). https://doi.org/10.1016/j.pep.2019.105524

[97] Mehta, S., Zhang, Y., Roth, R. H., Zhang, J. F., Mo, A., Tenner, B., et al. Single-fluorophore biosensors for sensitive and multiplexed detection of signalling activities. Nat. Cell Biol. 20, 1215–1225 (2018). https://doi.org/10.1038/s41556-018-0200-6
[98] Piatkevich, K. D., Jung, E. E., Straub, C., Linghu, C., Park, D., Suk, H., et al. A robotic multidimensional directed evolution approach applied to fluorescent voltage reporters. Nat. Chem. Biol. 14, 352–360 (2018). https://doi.org/10.1038/s41589-018-0004-9
[99] Goedhart, J., van Weeren, L., Hink, M. A., Vischer, N. O., Jalink, K., Gadella, T. W. Jr. Bright cyan fluorescent protein variants identified by fluorescence lifetime screening. Nat. Methods 7, 137–139 (2010). https://doi.org/10.1038/nmeth.1415
[100] Goedhart, J., von Stetten, D., Noirclerc-Savoye, M., Lelimousin, M., Joosen, L., Hink, M. A., et al. Structure-guided evolution of cyan fluorescent proteins towards a quantum yield of 93%. Nat. Commun. 3, 751 (2012). https://doi.org/10.1038/ncomms1738
[101] Bindels, D. S., Postma, M., Haarbosch, L., van Weeren, L., Gadella, T. W. J. Jr. Multiparameter screening method for developing optimized red-fluorescent proteins. Nat. Protoc. 15, 450–478 (2020). https://doi.org/10.1038/s41596-019-0250-7
[102] Kaur, H., Nguyen, K., Kumar, P. Pressure and temperature dependence of fluorescence anisotropy of green fluorescent protein. RSC Adv. 12, 8647–8655 (2022). https://doi.org/10.1039/d1ra08977c
[103] Tomosugi, W., Matsuda, T., Tani, T., Nemoto, T., Kotera, I., Saito, K., et al. An ultramarine fluorescent protein with increased photostability and pH insensitivity. Nat. Methods 6, 351–353 (2009). https://doi.org/10.1038/nmeth.1317
[104] Szymczak, A. L., Workman, C. J., Wang, Y., Vignali, K. M., Dilioglou, S., Vanin, E. F., et al. Correction of multi-gene deficiency in vivo using a single 'self-cleaving' 2A peptide-based retroviral vector. Nat. Biotechnol. 22, 589–594 (2004). https://doi.org/10.1038/nbt957
[105] Ai, H. W., Hazelwood, K. L., Davidson, M. W., Campbell, R. E. Fluorescent protein FRET pairs for ratiometric imaging of dual biosensors. Nat. Methods 5, 401–403 (2008). https://doi.org/10.1038/nmeth.1207
[106] Kremers, G. J., Goedhart, J., van Munster, E. B., Gadella, T. W. Jr. Cyan and yellow super fluorescent proteins with improved brightness, protein folding, and FRET Förster radius. Biochemistry 45, 6570–6580 (2006). https://doi.org/10.1021/bi0516273
[107] Shaner, N. C., Campbell, R. E., Steinbach, P. A., Giepmans, B. N., Palmer, A. E., Tsien, R. Y. Improved monomeric red, orange and yellow fluorescent proteins derived from Discosoma sp. red fluorescent protein. Nat. Biotechnol. 22, 1567–1572 (2004). https://doi.org/10.1038/nbt1037
[108] Yoshioka-Kobayashi, K., Matsumiya, M., Niino, Y., Isomura, A., Kori, H., Miyawaki, A., et al. Coupling delay controls synchronized oscillation in the segmentation clock. Nature 580, 119-123 (2020). https://doi.org/10.1038/s41586-019-1882-z
[109] Mittal, S., Chowhan, R. K., Singh, L. R. Macromolecular crowding: Macromolecules friend or foe. Biochim. Biophys. Acta. 1850, 1822–1831 (2015). http://doi.org/10.1016/j.bbagen.2015.05.002
[110] Saito, K., Nagai, T. Recent progress in luminescent proteins development. Curr. Opin. Chem. Biol. 27, 46–51 (2015). https://doi.org/10.1016/j.cbpa.2015.05.029
[111] Widder, E. A., Falls, B. Review of bioluminescence for engineers and scientists in biophotonics. IEEE J. Sel. Top. Quantum Electron. 20, 7100710 (2014). https://doi.org/10.1109/JSTQE.2013.2284434
[112] Hall, M. P., Unch, J., Binkowski, B. F., Valley, M. P., Butler, B. L., Wood, M. G., et al. Engineered luciferase reporter from a deep sea shrimp utilizing a novel imidazopyrazinone substrate. ACS Chem. Biol. 7, 1848–1857 (2012). https://doi.org/10.1021/cb3002478
[113] Saito, K., Chang, Y.-F., Horikawa, K., Hatsugai, N., Higuchi, Y., Hashida, M., et al. Luminescent proteins for high-speed single-cell and whole-body imaging. Nat. Commun. 3, 1262 (2012). https://doi.org/10.1038/ncomms2248
[114] Takai, A., Nakano, M., Saito, K., Haruno, R., Watanabe, T. M., Ohyanagi, T., et al. Expanded palette of Nano-lanterns for real-time multicolor luminescence imaging. Proc. Natl. Acad. Sci. U.S.A. 112, 4352–4356 (2015). https://doi.org/10.1073/pnas.1418468112
[115] Suzuki, K., Kimura, T., Shinoda, H., Bai, G., Daniels, M. J., Arai, Y., et al. Five colour variants of bright luminescent protein for real-time multicolour bioimaging. Nat. Commun. 7, 13718 (2016). https://doi.org/10.1038/ncomms13718
[116] Suzuki, K., Nagai, T. Recent progress in expanding the chemiluminescent toolbox for bioimaging. Curr. Opin. Biotechnol. 48, 135–141 (2017). https://doi.org/10.1016/j.copbio.2017.04.001
[117] Rumble, J. CRC handbook of chemistry and physics, 102nd Ed. (CRC Press, Boca Raton, 2021).
[118] ElAfandy, R. T., AbuElela, A. F., Mishra, P., Janjua, B., Oubei, H. M., Büttner, U., et al. Nanomembrane-based, thermal-transport biosensor for living cells. Small. 13, 1603080 (2017). https://doi.org/10.1002/smll.201603080

[119] Inomata, N., Miyamoto, T., Okabe, K., Ono, T. Measurement of cellular thermal properties and their temperature dependence based on frequency spectra via an on-chip-integrated microthermistor. Lab Chip. 23, 2411–2420 (2023). https://doi.org/10.1039/d2lc01185a
[120] Sotoma, S., Zhong, C., Kah, J. C. Y., Yamashita, H., Plakhotnik, T., Harada, Y., et al. In situ measurements of intracellular thermal conductivity using heater-thermometer hybrid diamond nanosensors. Sci. Adv. 7, eabd7888 (2021). https://doi.org/10.1126/sciadv.abd7888
[121] Crank, J. The mathematics of diffusion, 2nd Ed. (Oxford University Press, Oxford, 1975).
[122] Lervik, A., Bresme, F., Kjelstrup, S., Bedeaux, D., Rubi, J. M. Heat transfer in protein-water interfaces. Phys. Chem. Chem. Phys. 12, 1610–1617 (2010). https://doi.org/10.1039/b918607g
[123] Yang, P. H., Rupley, J. A. Protein-water interactions. Heat capacity of the lysozyme-water system. Biochemistry 18, 2654–2661 (1979). https://doi.org/10.1021/bi00579a035
[124] Iqbal, M., Ronald, E., Verrall, R. E. Volumetric properties of aqueous solutions of bovine serum albumin, human serum albumin, and human hemoglobin. J. Phys. Chem. 91, 1935–1941 (1987). https://doi.org/10.1021/j100291a050
[125] Bastos, A. R. N., Brites, C. D. S., Rojas-Gutierrez, P. A., DeWolf, C., Ferreira, R. A. S., Capobianco, J. A., et al. Thermal properties of lipid bilayers determined using upconversion nanothermometry. Adv. Funct. Mater. 29, 1905474 (2019). https://doi.org/10.1002/adfm.201905474
[126] Blume, A. Apparent molar heat capacities of phospholipids in aqueous dispersion. Effects of chain length and head group structure. Biochemistry 22, 5436–5442 (1983). https://doi.org/10.1021/bi00292a027
[127] Suzuki, M., Plakhotnik, T. The challenge of intracellular temperature. Biophys. Rev. 12, 593–600 (2020). https://doi.org/10.1007/s12551-020-00683-8
[128] Baffou, G., Rigneault, H., Marguet, D., Jullien, L. A critique of methods for temperature imaging in single cells. Nat. Methods 11, 899–901 (2014). https://doi.org/10.1038/nmeth.3073
[129] Suzuki, M., Zeeb, V., Arai, S., Oyama, K., Ishiwata, S. The 10^5 gap issue between calculation and measurement in single-cell thermometry. Nat. Methods 12, 802–803 (2015). https://doi.org/10.1038/nmeth.3551
[130] Rajagopal, M. C., Brown, J. W., Gelda, D., Valavala, K. V., Wang, H., Llano, D. A., et al. Transient heat release during induced mitochondrial proton uncoupling. Commun. Biol. 2, 279 (2019). https://doi.org/10.1038/s42003-019-0535-y
[131] Sato, M. K., Toda, M., Inomata, N., Maruyama, H., Okamatsu-Ogura, Y., Arai, F., et al. Temperature changes in brown adipocytes detected with a bimaterial microcantilever. Biophys. J. 106, 2458–2464 (2014). https://doi.org/10.1016/j.bpj.2014.04.044
[132] Sugimura, T., Kajimoto, S., Nakabayashi, T. Label-free imaging of intracellular temperature by using the O-H stretching raman band of water. Angew. Chem. Int. Ed. Engl. 59, 7755–7760 (2020). https://doi.org/10.1002/anie.201915846
[133] Piñol, R., Zeler, J., Brites, C. D. S., Gu, Y., Téllez, P., Carneiro Neto, A. N., et al. Real-time Intracellular temperature imaging using lanthanide-bearing polymeric micelles. Nano Lett. 20, 6466–6472 (2020). https://doi.org/10.1021/acs.nanolett.0c02163
[134] Chuma, S., Kiyosue, K., Akiyama, T., Kinoshita, M., Shimazaki, Y., Uchiyama, S., et al. Implication of thermal signaling in neuronal differentiation revealed by manipulation and measurement of intracellular temperature. Nat. Commun. 15, 3473 (2024). https://doi.org/10.1038/s41467-024-47542-8
[135] Chrétien, D., Bénit, P., Ha, H. H., Keipert, S., El-Khoury, R., Chang, Y. T., et al. Mitochondria are physiologically maintained at close to 50 °C. PLoS Biol. 16, e2003992 (2018). https://doi.org/10.1371/journal.pbio.2003992
[136] Chrétien, D., Bénit, P., Leroy, C., El-Khoury, R., Park, S., Lee, J. Y., et al. Pitfalls in monitoring mitochondrial temperature using charged thermosensitive fluorophores. Chemosensors 8, 124 (2020). http://doi.org/10.3390/chemosensors8040124
[137] Terzioglu, M., Veeroja, K., Montonen, T., Ihalainen, T. O., Salminen, T. S., Bénit, P., et al. Mitochondrial temperature homeostasis resists external metabolic stresses. eLife 12, RP89232 (2023). https://doi.org/10.7554/eLife.89232
[138] Fahimi, P., Matta, C. F. The hot mitochondrion paradox: Reconciling theory and experiment. Trends Chem. 4, 96–110 (2022). https://doi.org/10.1016/j.trechm.2021.10.005
[139] Chung, C. W., Stephens, A. D., Konno, T., Ward, E., Avezov, E., Kaminski, C. F., et al. Intracellular Aβ42 aggregation leads to cellular thermogenesis. J. Am. Chem. Soc. 144, 10034–10041 (2022). https://doi.org/10.1021/jacs.2c03599
[140] Bakken, G. S., Krochmal, A. R. The imaging properties and sensitivity of the facial pits of pitvipers as determined by optical and heat-transfer analysis. J. Exp. Biol. 210, 2801–2810 (2007). https://doi.org/10.1242/jeb.006965
[141] Gracheva, E. O., Ingolia, N. T., Kelly, Y. M., Cordero-Morales, J. F., Hollopeter, G., Chesler, A. T., et al. Molecular basis of infrared detection by snakes. Nature 464, 1006–1011 (2010).

https://doi.org/10.1038/nature08943
[142] Graf, I. R., Machta, B. B. A bifurcation integrates information from many noisy ion channels and allows for milli-Kelvin thermal sensitivity in the snake pit organ. Proc. Natl. Acad. Sci. U.S.A. 121, e2308215121 (2024). https://doi.org/10.1073/pnas.2308215121
[143] Ferdinandus, Suzuki, M., Vu, C. Q., Harada, Y., Sarker, S. R., Ishiwata, S., et al. Modulation of local cellular activities using a photothermal dye-based subcellular-sized heat spot. ACS Nano 16, 9004–9018 (2022). https://doi.org/10.1021/acsnano.2c00285
[144] Hille, B. Ion channels of excitable membranes, 3rd Ed. (Sinauer, Sunderland, 2001).